



# Augmented Lagrangian method for constraining the shape of velocity profiles at outlet boundaries for three-dimensional finite element simulations of blood flow

H.J. Kim<sup>a</sup>, C.A. Figueroa<sup>b</sup>, T.J.R. Hughes<sup>c</sup>, K.E. Jansen<sup>d</sup>, C.A. Taylor<sup>b,\*</sup>

<sup>a</sup> Department of Mechanical Engineering, Stanford University, E350 Clark Center, 318 Campus Drive, Stanford, CA 94305, USA

<sup>b</sup> Department of Bioengineering, Stanford University, E350 Clark Center, 318 Campus Drive, Stanford, CA 94305, USA

<sup>c</sup> Institute for Computational Engineering and Sciences, The University of Texas at Austin, 201 East 24th Street, ACES 5.430A 1 University Station, C0200, Austin, TX 78712, USA

<sup>d</sup> Scientific Computation Research Center and the Department of Mechanical, Aeronautical and Nuclear Engineering, Rensselaer Polytechnic Institute, Troy, NY 12180, USA

## ARTICLE INFO

### Article history:

Received 19 April 2008

Received in revised form 3 February 2009

Accepted 7 February 2009

Available online 20 February 2009

### Keywords:

Blood flow

Boundary conditions

Augmented Lagrangian method

Coupled Multidomain Method

## ABSTRACT

In three-dimensional blood flow simulations of the cardiovascular system, velocity and pressure fields in the computational domain are highly affected by outlet boundary conditions. This fact has motivated the development of novel methods to couple three-dimensional computational domains with one-dimensional numerical models or, alternatively, with zero-dimensional or one-dimensional analytic models. In all such methods described to date, whether they are explicit or implicit, the relationship between flow and pressure at the outlet boundary is enforced weakly. This coupling does not include any constraints on the shape of the velocity profiles nor on the distribution of pressure at the interface. As a result, there remain some classes of problems that are, at best, difficult to solve, and at worst, intractable, with current numerical methods for simulating blood flow. These include problems with significant flow reversal during part of the cardiac cycle or geometric complexity in the proximity of the outlet of the computational domain. We have implemented a novel method to resolve these challenging problems whereby an augmented Lagrangian method is used to enforce constraints on the shape of the velocity profile at the interface between the upstream computational domain and the downstream analytic domain. These constraints on the shape of the velocity profile are added to the Coupled Multidomain Method in order to implicitly couple the computational domain with downstream analytic models. In this study, an axisymmetric profile is imposed after ensuring that each constrained outlet boundary is circular. We demonstrate herein that including constraints on the shape of the velocity profile does not affect velocity and pressure fields except in the immediate vicinity of the constrained outlet boundaries. Furthermore, this new method enables the solution of problems which diverged with an unconstrained method.

© 2009 Published by Elsevier B.V.

## 1. Introduction

Computational simulations have evolved as a powerful tool for quantifying blood flow and pressure of the cardiovascular system [47] in studies of the hemodynamics of healthy and diseased blood vessels [3,23,25,33,34,38,44,48,53,56], the design and evaluation of medical devices, [14,27,43] and prediction of the outcomes of surgeries [24,28,29,40,46]. As computing power and numerical methods advance, simulation-based methods are expected to become even more extensively used in studying the cardiovascular system. In recent years, much progress has been made in simulating blood flow in arteries, especially in boundary condition development. Previously, constant or time-varying pressure, zero traction or velocity were utilized as outlet boundary conditions [3,14,23,24,27,33,34,40,43,44,46,48,53]. Such boundary conditions are limiting in that they do not accurately replicate vascular

impedance of the downstream vasculature. More recently, new outlet boundary conditions have been developed in an effort to better model the interactions between the computational domain and the downstream vasculature. The new outlet boundary conditions couple the computational domain with simpler models such as resistance, impedance, lumped-parameter models, or one-dimensional models [1,7–11,25,28,29,36,38,49–52,56]. With this coupling, outlet boundary conditions are derived naturally through the interactions between the computational domain and downstream analytic or computational models, thus enabling highly realistic flow rate and pressure fields. We previously developed a highly versatile method, the Coupled Multidomain Method [51,52], to couple a three-dimensional finite element model of the cardiovascular system to a variety of downstream analytic models. The Coupled Multidomain Method enabled us to obtain physiologically realistic flow rate and pressure.

However, we have encountered two remaining challenges in prescribing outlet boundary conditions for three-dimensional simulations of blood flow. The first challenge occurs when complex

\* Corresponding author. Tel.: +1 650 725 6128; fax: +1 650 725 9082

E-mail address: [taylorca@stanford.edu](mailto:taylorca@stanford.edu) (C.A. Taylor).

flow structures propagate to the outlet boundary due to vessel curvature or branches immediately upstream of the outlet boundary. This problem can often be resolved by artificially extending the vessel with a long, straight segment. Yet, the addition of this segment creates an artificial and non-physiologic part in the computational domain and can cause a significant part of the computational domain to reside in regions of no interest. The second challenge occurs in modeling problems including branches off of the arch of the aorta, the infra-renal segment of the aorta, and the lower extremity vessels due to significant retrograde flow through these vessels during part of the cardiac cycle [45]. As flow is drawn back into the computational domain from the downstream analytic models, the velocity distribution at the interface becomes irregular and, in many cases, results in a divergence of the simulation.

These challenges occur because outlet boundary conditions which involve coupling between a three-dimensional domain and a zero-dimensional or one-dimensional model, including the Coupled Multidomain Method, generally impose weak relationships between flow and pressure at each interface. This coupling does not include any constraints on the shape of velocity profiles nor on the pressure distribution at the interface. Yet, zero-dimensional and one-dimensional models are derived based on an assumed shape of the velocity profile and the assumption of uniform pressure over the cross section [5,20,55]. Therefore, the coupling of the three-dimensional domain and a zero-dimensional or one-dimensional model is not consistent if the three-dimensional domain has no constraints on the shape of the velocity profiles and pressure distribution at the interface.

There have been studies to resolve challenges associated with outlet boundary conditions in computational hemodynamics. Formaggia et al. [9] implemented a total pressure boundary condition by constructing a special formulation of the Navier–Stokes equations. The total pressure boundary condition controls the energy flux entering and exiting the computational domain, thus, stabilizes fluid dynamics problems by setting energy bounds. However, this approach requires an unconventional formulation of the Navier–Stokes equations and it remains to be seen whether it will address all of the numerical difficulties associated with complex flows at boundaries.

In this paper, we add constraints on the shape of velocity profiles to the formulation of the Coupled Multidomain Method. These additional constraints can be readily implemented in flow solvers that use standard formulations of the Navier–Stokes equations. Additionally, by constraining the shape of velocity profiles, we achieve consistent coupling between the three-dimensional domain and a zero-dimensional or one-dimensional model.

In finite element methods, constraints are generally enforced using penalty methods or Lagrange multiplier methods [21]. Both of these methods are used in a variety of applications, among them, to enforce incompressibility in a computational domain or mass flux through the boundary [8,11,31,50]. An augmented Lagrangian method enforces constraints using both penalty and Lagrange multiplier methods, and can be used to achieve faster convergence and enforce constraints more strongly [12,15,17,35,39]. To our knowledge, penalty methods, Lagrange multiplier methods, and augmented Lagrangian methods have not been applied in computational fluid dynamic studies to enforce constraints on the shape of velocity profiles. We utilize an augmented Lagrangian method to weakly enforce the shape of velocity profiles at outlet boundaries. By constraining the shape of velocity profiles, we obtain solutions of problems which diverged with an unconstrained method.

This paper is organized as follows. First, we present the derivation of an augmented Lagrangian method for constraining the shape of velocity profiles of outlet boundaries and describe constraint and velocity profile functions. We then demonstrate this method by applying it to simulate blood flow in a straight cylindrical

model and a subject-specific abdominal aorta model and show that this new method does not affect velocity and pressure except in the immediate vicinity of the outlet boundary. We next use an idealized aortic bifurcation model to illustrate that this method can be used to truncate branch vessels very close to a vessel of interest. Finally, we demonstrate the utility of this method by using it to compute pulsatile flow in a subject-specific thoracic aorta model where there is significant retrograde flow during early diastole.

## 2. Methods

### 2.1. Governing equations (strong form)

Blood flow in the large vessels of the cardiovascular system can be approximated as the flow of an incompressible Newtonian fluid [34] in domain  $\Omega \in R^{n_{sd}}$  where  $n_{sd}$  is the number of spatial dimensions. Boundary  $\Gamma$  of spatial domain  $\Omega$  is split into Dirichlet partition  $\Gamma_g$  and Neumann partition  $\Gamma_h$  such that  $\Gamma = \partial\Omega = (\Gamma_g \cup \Gamma_h)$  and  $\Gamma_g \cap \Gamma_h = \emptyset$ .

The three-dimensional equations of an incompressible Newtonian fluid consist of the three momentum balance equations and the continuity equation with suitable boundary and initial conditions:

$$\rho \vec{v}_{,t} + \rho \vec{v} \cdot \nabla \vec{v} = -\nabla p + \text{div}(\underline{\tau}) + \vec{f},$$

$$\text{div}(\vec{v}) = 0, \quad (1)$$

$$\text{where } \underline{\tau} = 2\mu \underline{\mathcal{D}} \quad \text{with } \underline{\mathcal{D}} = \frac{1}{2}(\nabla \vec{v} + \nabla \vec{v}^T),$$

$$\vec{v}(\vec{x}, t) = \vec{g}(\vec{x}, t), \quad \vec{x} \in \Gamma_g, \quad (2)$$

$$\vec{t}_{\vec{n}} = [-p \vec{I} + \underline{\tau}] \cdot \vec{n} = \vec{h}(\vec{v}, p, \vec{x}, t), \quad \vec{x} \in \Gamma_h, \quad (3)$$

$$\vec{v}(\vec{x}, 0) = \vec{v}_0(\vec{x}), \quad \vec{x} \in \Omega. \quad (4)$$

The unknowns are fluid velocity  $\vec{v} = (v_x, v_y, v_z)$  and pressure  $p$ . Density  $\rho$  and viscosity  $\mu$  of the fluid are assumed to be constant.  $\vec{f}$  is the external body force.

Constraint functions are designed to enforce a shape of the velocity profile on a part of Neumann partition  $\Gamma_h$ . For each constrained face  $\Gamma_{h_k}$ , where  $\Gamma_{h_k} \subseteq \Gamma_h$ , the following constraint functions are imposed:

$$c_{k1}(\vec{v}, \vec{x}, t) = \alpha_k \int_{\Gamma_{h_k}} (\vec{v}(\vec{x}, t) \cdot \vec{n} - \Phi_k(\vec{v}(\vec{x}, t), \vec{x}, t))^2 ds = 0,$$

$$c_{k2}(\vec{v}, \vec{x}, t) = \alpha_k \int_{\Gamma_{h_k}} (\vec{v}(\vec{x}, t) \cdot \vec{t}_2)^2 ds = 0, \quad (5)$$

$$c_{k3}(\vec{v}, \vec{x}, t) = \alpha_k \int_{\Gamma_{h_k}} (\vec{v}(\vec{x}, t) \cdot \vec{t}_3)^2 ds = 0 \quad \text{for } k = 1, \dots, n_c, \quad \vec{x} \in \Gamma_{h_k}.$$

Here,  $n_c$  is the number of faces where the constraints on the shape of the velocity profile are enforced, and  $\Phi_k(\vec{v}(\vec{x}, t), \vec{x}, t)$  is the desired shape of the normal velocity profile. Note that although the shape of the velocity profile is constant, the velocity profile itself changes as the flow rate at face  $\Gamma_{h_k}$  changes. Here,  $\vec{n}$  is the unit normal vector of face  $\Gamma_{h_k}$ ,  $\vec{t}_2$  and  $\vec{t}_3$  are unit in-plane vectors that are orthogonal to each other and to the unit normal vector  $\vec{n}$  at face  $\Gamma_{h_k}$ .  $\alpha_k$  is used to nondimensionalize the constraint functions:

$$\alpha_k = \frac{\int_{\Gamma_{h_k}} ds}{Q_k^2}, \quad (6)$$

where  $\bar{Q}_k$  is the mean flow of face  $\Gamma_{h_k}$ .

The instability occurring in blood flow simulations with retrograde flow can be explained with a classical stability analysis derived from the Navier–Stokes equations:

$$\begin{aligned} & \frac{\rho}{2} \int_{\Omega} (\vec{v} \cdot \vec{v})_t d\vec{x} + \int_{\Omega} \nabla \vec{v} : \tau d\vec{x} \\ &= \int_{\Gamma_g} \vec{g} \cdot \left( -\left( p + \frac{\rho}{2} \vec{g} \cdot \vec{g} \right) \vec{I} + \tau \right) \cdot \vec{n} ds - \frac{\rho}{2} \int_{\Gamma_h} (\vec{v} \cdot \vec{v}) \vec{v} \cdot \vec{n} ds \\ &+ \int_{\Gamma_h} \vec{h} \cdot \vec{v} ds + \int_{\Omega} \vec{f} \cdot \vec{v} d\vec{x}. \end{aligned}$$

$\int_{\Gamma_g} \vec{g} \cdot \left( -\left( p + \frac{\rho}{2} \vec{g} \cdot \vec{g} \right) \vec{I} + \tau \right) \cdot \vec{n} d\Gamma$  is bounded as these values are derived from a Dirichlet boundary condition. However, for Neumann boundary conditions, if  $\vec{v} \cdot \vec{n}|_{\Gamma_h} < 0$ ,  $-\frac{\rho}{2} \int_{\Gamma_h} (\vec{v} \cdot \vec{v}) \vec{v} \cdot \vec{n} d\Gamma$  is positive and destabilizing. We can decompose the destabilizing term  $\frac{\rho}{2} \int_{\Gamma_h} (\vec{v} \cdot \vec{v}) \vec{v} \cdot \vec{n} d\Gamma$  as follows:

$$\begin{aligned} \frac{\rho}{2} \int_{\Gamma_h} (\vec{v} \cdot \vec{v}) \vec{v} \cdot \vec{n} d\Gamma &= \frac{\rho}{2} \int_{\Gamma_h} (\vec{v}_n \cdot \vec{v}_n + \vec{v}_\tau \cdot \vec{v}_\tau) \vec{v} \cdot \vec{n} d\Gamma, \quad \text{where } \vec{v}_n \\ &= (\vec{v} \cdot \vec{n}) \vec{n}, \quad \vec{v}_\tau = \vec{v} - \vec{v}_n. \end{aligned}$$

To stabilize this destabilizing term, we need to bound  $\vec{v}_n \cdot \vec{v}_n$ ,  $\vec{v}_\tau \cdot \vec{v}_\tau$ , and  $\vec{v} \cdot \vec{n}$ . The continuity equation controls the total flux through the boundaries, thus controlling the magnitude of  $\vec{v} \cdot \vec{n}$ . However, this control is not strong enough to stabilize the problems in blood flow simulations as it controls the total flux, not the flux through each boundary. The constraint function  $c_{k1}$  controls normal velocity components of each boundary providing stronger constraints on the boundary flux. The continuity equation and the constraint function  $c_{k1}$  together control the magnitudes of  $\vec{v}_n \cdot \vec{v}_n$  and  $\vec{v} \cdot \vec{n}$ . The other two constraint functions  $c_{k2}$  and  $c_{k3}$  minimize in-plane velocity components, and thus bound  $\vec{v}_\tau \cdot \vec{v}_\tau$ . Therefore, our proposed method stabilizes the instability that can arise with retrograde flow.

### 2.2. Governing equations (weak form)

The trial solution and weighting function spaces for the semi-discrete formulation of the momentum balance, continuity, and constraint equations are defined as follows:

$$\begin{aligned} \mathcal{S} &= \left\{ \vec{v} | \vec{v}(\cdot, t) \in H^1(\Omega)^{n_{sd}}, t \in [0, T], \vec{v}(\cdot, t) = \vec{g} \text{ on } \Gamma_g \right\}, \\ \mathcal{W} &= \left\{ \vec{w} | \vec{w}(\cdot, t) \in H^1(\Omega)^{n_{sd}}, t \in [0, T], \vec{w}(\cdot, t) = \vec{0} \text{ on } \Gamma_g \right\}, \\ \mathcal{P} &= \left\{ p | p(\cdot, t) \in H^1(\Omega), t \in [0, T] \right\}, \\ \vec{\lambda}_1(t), \vec{\lambda}_2(t), \dots, \vec{\lambda}_{n_c}(t) &\in (L^2(0, T))^{n_{sd}}, \\ \delta \vec{\lambda}_1(t), \delta \vec{\lambda}_2(t), \dots, \delta \vec{\lambda}_{n_c}(t) &\in (L^2(0, T))^{n_{sd}}, \\ \vec{\kappa}_k &\in \mathcal{R}^{n_{sd}}, \text{ Penalty numbers where } k = 1, \dots, n_c, \\ \vec{\sigma}_k &\in \mathcal{R}^{n_{sd}}, \text{ Regularization parameters such that } |\vec{\sigma}_k| \ll 1, \\ &k = 1, \dots, n_c. \end{aligned} \tag{7}$$

Here,  $H^1(\Omega)$  represents the Sobolev space of functions which are square-integrable in  $\Omega$  and whose first derivatives are also square-integrable in  $\Omega$ .  $L^2(0, T)$  represents the Hilbert space of functions that are square-integrable in time  $(0, T)$ .  $n_{sd}$  is the number of spatial dimensions and is assumed to be three.  $\vec{g}$  is the assigned Dirichlet boundary condition and  $\vec{\lambda}_k(t)$  and  $\delta \vec{\lambda}_k(t)$  are the Lagrange multipliers and the test functions of the Lagrange multipliers, respectively. Penalty numbers  $\vec{\kappa}_k$  are added for the augmented Lagrangian method [12,15,17,35] to penalize the constraint functions. Regularization parameters  $\vec{\sigma}_k$  are utilized to regularize the constraint equations. The regularization is needed to prevent the formulation of an ill-conditioned system of equations. In Hughes [21], incompressible behavior in elasticity theory is regularized by replacing it with slightly compressible behavior, in which case the

Lagrange multipliers play the role of pressure and the regularization parameters play the role of an artificial compliance. Analogously, the regularization parameters can be considered a normalized artificial velocity and the Lagrange multipliers a normalized artificial force.

The weak form becomes:

Find  $\vec{v} \in \mathcal{S}$ ,  $p \in \mathcal{P}$  and  $\vec{\lambda}_1, \vec{\lambda}_2, \dots, \vec{\lambda}_{n_c} \in (L^2(0, T))^{n_{sd}}$  such that for any  $\vec{w} \in \mathcal{W}$ ,  $q \in \mathcal{P}$  and  $\delta \vec{\lambda}_1, \delta \vec{\lambda}_2, \dots, \delta \vec{\lambda}_{n_c} \in (L^2(0, T))^{n_{sd}}$  the following is satisfied:

$$\begin{aligned} B_C(\vec{w}, q, \delta \vec{\lambda}_1, \dots, \delta \vec{\lambda}_{n_c}; \vec{v}, p, \vec{\lambda}_1, \dots, \vec{\lambda}_{n_c}) &= \int_{\Omega} \left\{ \vec{w} \cdot (\rho \vec{v}_t + \rho \vec{v} \cdot \nabla \vec{v} - \vec{f}) + \nabla \vec{w} : (-p \vec{I} + \tau) \right\} d\vec{x} \\ &- \int_{\Omega} \nabla q \cdot \vec{v} d\vec{x} - \int_{\Gamma_h} \vec{w} \cdot (-p \vec{I} + \tau) \cdot \vec{n} ds + \int_{\Gamma} q \vec{v} \cdot \vec{n} ds \\ &+ \sum_{i=1}^{n_{sd}} \sum_{k=1}^{n_c} \left\{ \lambda_{ki} \cdot (\sigma_{ki} \delta \lambda_{ki} - \delta c_{ki}(\vec{w}; \vec{v}, \vec{x}, t)) \right\} + \sum_{i=1}^{n_{sd}} \sum_{k=1}^{n_c} \delta \lambda_{ki} \cdot (\sigma_{ki} \lambda_{ki} - c_{ki}(\vec{v}, \vec{x}, t)) \\ &+ \sum_{i=1}^{n_{sd}} \sum_{k=1}^{n_c} \kappa_{ki} \cdot c_{ki}(\vec{v}, \vec{x}, t) \delta c_{ki}(\vec{w}; \vec{v}, \vec{x}, t) = 0, \end{aligned}$$

$$\text{where } \delta c_{ki}(\vec{w}; \vec{v}, \vec{x}, t) = \lim_{\epsilon \rightarrow 0} \frac{dc_{ki}(\vec{v} + \epsilon \vec{w}, \vec{x}, t)}{d\epsilon}. \tag{8}$$

This formulation can be considered a traditional Galerkin weak form in addition to new constraint terms that are obtained by the minimization of the following terms on a portion of the Neumann boundary:

$$\begin{aligned} &- \sum_{i=1}^{n_{sd}} \sum_{k=1}^{n_c} \left\{ \lambda_{ki} \cdot c_{ki}(\vec{v}, \vec{x}, t) \right\} + \frac{1}{2} \sum_{i=1}^{n_{sd}} \sum_{k=1}^{n_c} \kappa_{ki} \cdot c_{ki}(\vec{v}, \vec{x}, t)^2 \\ &+ \text{sum}_{i=1}^{n_{sd}} \sum_{k=1}^{n_c} \sigma_{ki} \lambda_{ki}^2, \end{aligned} \tag{9}$$

where  $\sum_{i=1}^{n_{sd}} \sum_{k=1}^{n_c} \left\{ \lambda_{ki} \cdot c_{ki}(\vec{v}, \vec{x}, t) \right\}$  is the Lagrange multiplier term whereas  $\frac{1}{2} \sum_{i=1}^{n_{sd}} \sum_{k=1}^{n_c} \kappa_{ki} \cdot c_{ki}(\vec{v}, \vec{x}, t)^2$  is the penalty term. In addition to the terms required to impose the augmented Lagrangian method, the regularization term  $\sum_{i=1}^{n_{sd}} \sum_{k=1}^{n_c} \sigma_{ki} \lambda_{ki}^2$  is added to obtain a system of equations with a non-zero diagonal block for the Lagrange multiplier degrees of freedom. The regularization parameters are chosen to be  $\sigma_{ki} \ll \frac{c_{ki}}{\lambda_{ki}}$  such that the regularization term remains small compared to the Lagrange multiplier and penalty terms of the augmented Lagrangian method. With the regularization term introduced, we ensure that the system of equations is well-conditioned and can be solved for velocity and pressure fields only by explicitly expressing the increments of the Lagrange multipliers as a function of the increments of velocity and pressure. This will be further explained later.

The Neumann boundary generally consists of the outlets, and if the deformability of the blood vessels is considered, the lateral surface of the domain is added to the Neumann boundary [6]. For outlet boundary conditions, resistance, impedance, and three-element Windkessel models are implemented using the Coupled Multidomain Method [51,52]. In the Coupled Multidomain Method, operators  $M = [M_m, \vec{M}_c]$  and  $H = [H_m, \vec{H}_c]$  are defined to represent the traction tensor and velocity at the outlet boundaries as follows:

$$\begin{aligned} (-p \vec{I} + \tau)|_{\Gamma_h} &\approx [M_m(\vec{v}, p) + H_m]_{\Gamma_h} \\ \vec{v}|_{\Gamma_h} &\approx [\vec{M}_c(\vec{v}, p) + \vec{H}_c]_{\Gamma_h} \end{aligned} \tag{10}$$

These operators  $M$  and  $H$  are defined from analytic models representing downstream vasculatures. The resulting weak form becomes:

$$\begin{aligned}
 & B_G(\vec{w}, q, \delta\vec{\lambda}_1, \dots, \delta\vec{\lambda}_{n_c}; \vec{v}, p, \vec{\lambda}_1, \dots, \vec{\lambda}_{n_c}) \\
 &= \int_{\Omega} \left\{ \vec{w} \cdot (\rho \vec{v}_{,t} + \rho \vec{v} \cdot \nabla \vec{v} - \vec{f}) + \nabla \vec{w} : (-pI + \underline{\tau}) \right\} d\vec{x} \\
 &\quad - \int_{\Omega} \nabla q \cdot \vec{v} d\vec{x} - \int_{\Gamma_h} \vec{w} \cdot (\underline{M}_m(\vec{v}, p) + \underline{H}_m) \cdot \vec{n} ds \\
 &\quad + \int_{\Gamma_h} q (\underline{M}_c(\vec{v}, p) + \underline{H}_c) \cdot \vec{n} ds + \int_{\Gamma_g} q \vec{v} \cdot \vec{n} ds \\
 &\quad + \left[ \sum_{i=1}^{n_{sd}} \sum_{k=1}^{n_c} \{ \lambda_{ki} \delta \lambda_{ki} - \delta c_{ki}(\vec{w}; \vec{v}, \vec{x}, t) \} + \sum_{i=1}^{n_{sd}} \sum_{k=1}^{n_c} \delta \lambda_{ki} \cdot (\sigma_{ki} \lambda_{ki} - c_{ki}(\vec{v}, \vec{x}, t)) \right] \\
 &\quad + \left[ \sum_{i=1}^{n_{sd}} \sum_{k=1}^{n_c} K_{ki} \cdot c_{ki}(\vec{v}, \vec{x}, t) \delta c_{ki}(\vec{w}; \vec{v}, \vec{x}, t) \right] = 0. \tag{11}
 \end{aligned}$$

For the vessel wall boundary, the Coupled Momentum Method can be utilized to model the fluid–solid interaction between blood flow and elastic vessel walls [6].

### 2.3. Velocity profile function

The shape of the normal velocity profile of outlet boundary  $\Gamma_{h_k}$  is determined by the function  $\Phi_k(\vec{v}(\vec{x}, t), \vec{x}, t)$ . Function  $\Phi_k(\vec{v}(\vec{x}, t), \vec{x}, t)$  is a function of the flow rate and the prescribed shape of the normal velocity profile. In this function, the flow rate is unknown and is derived through the interactions between the three-dimensional domain and the downstream domains. However, the shape of the velocity profile,  $\varphi_k$ , can be determined once the geometry of the constrained surface is known. Thus, function  $\Phi_k(\vec{v}(\vec{x}, t), \vec{x}, t)$  can be determined using the known profile function  $\varphi_k$  and an unknown flow rate. Profile function  $\varphi_k$  is scaled depending on the resulting flow rate:

$$\Phi_k(\vec{v}(\vec{x}, t), \vec{x}, t) = \frac{\int_{\Gamma_{h_k}} \vec{v} \cdot \vec{n} ds}{\int_{\Gamma_{h_k}} ds} \varphi_k(\vec{x}, t). \tag{12}$$

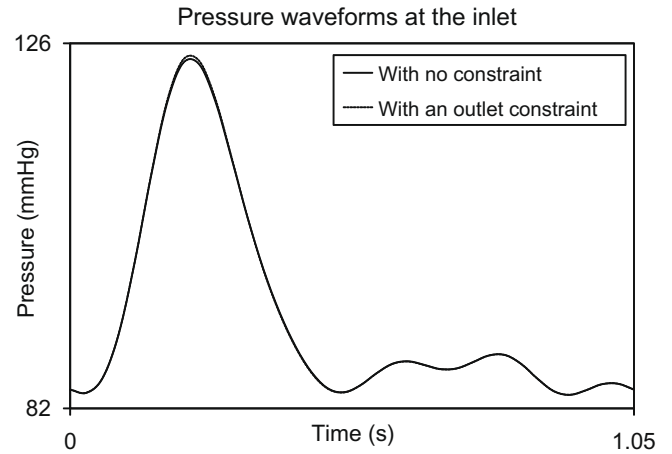


Fig. 2. Comparison of inlet pressure waveforms of a straight cylindrical model with a Womersley inlet velocity and impedance outlet boundary conditions for simulations with and without constraints on the shape of the outlet velocity profile.

In this study, we ensure that the boundary face is circular and impose an axisymmetric profile function [20] as the following:

$$\varphi(r) = \frac{n+2}{n} \left( 1 - \left( \frac{r}{R} \right)^n \right), \tag{13}$$

where  $n$  is an integer greater than one,  $r$  is the distance between a point on the face and the center and  $R$  is the radius of the face. Note that when  $n = 2$ , the profile function is parabolic. The order of the profile function can be optimized to give a minimal difference between the profile function and a Womersley profile [55] based on the geometry and pulsatility of the inflow for the problem. The assumption of circular faces and the above choice of profile function were made without loss of generality.

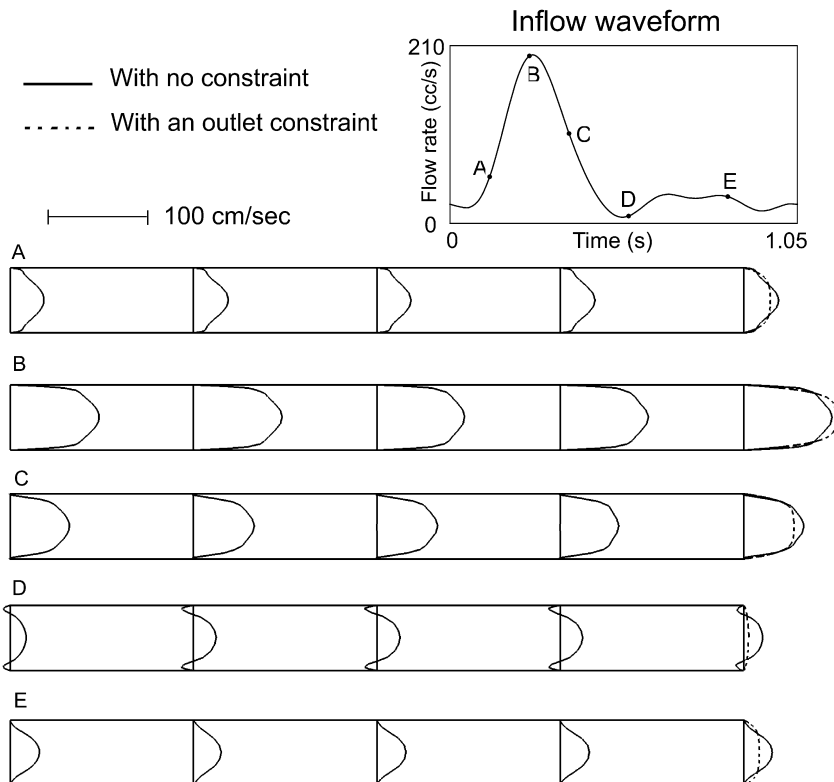


Fig. 1. Velocity profiles at five different axial locations for five different time points of a straight cylindrical model with a Womersley inlet velocity and impedance outlet boundary conditions. Note that for all axial locations except the outlet, the velocity profiles for the unconstrained and constrained solutions are indistinguishable.

2.4. Finite element discretization

In this study, we employ a stabilized semi-discrete finite element method, based on the ideas developed in Brooks and Hughes

[2], Franca and Frey [13], Taylor et al. [48], and Whiting et al [54]. The discrete trial solution and weighting function spaces for the semi-discrete formulation are as follows:

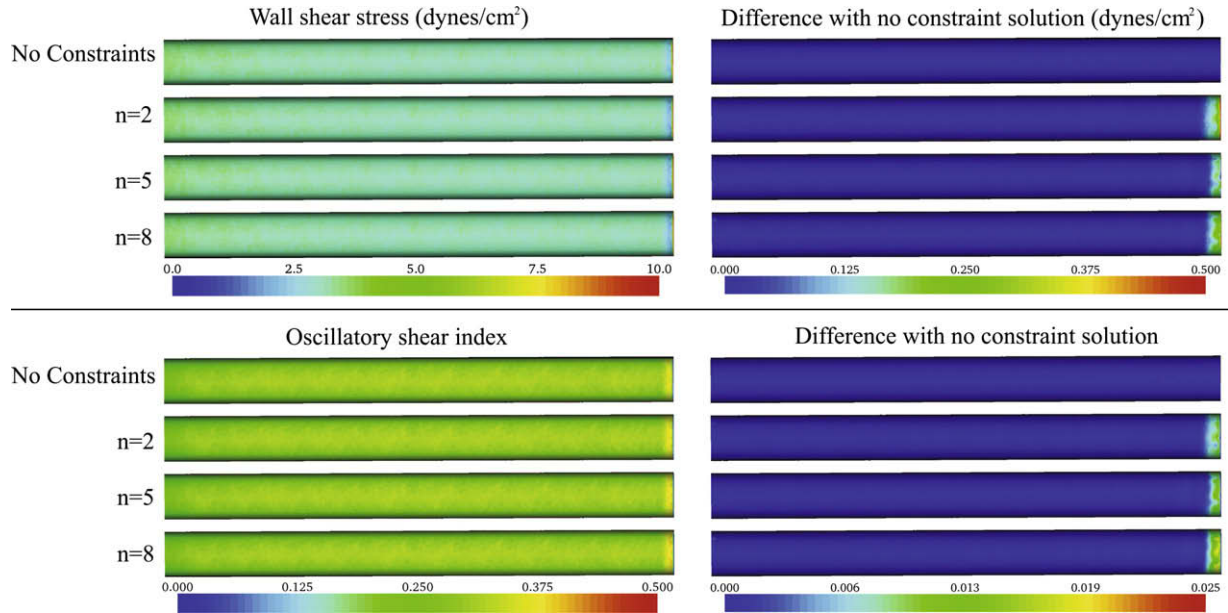


Fig. 3. Comparison of mean wall shear stress and oscillatory shear index of a straight cylindrical model with a Womersley inlet velocity and impedance outlet boundary conditions for simulations with and without constraints on the shape of the outlet velocity profile. For simulations with constraints, different profile orders of  $n = 2, 5, 8$  are used.

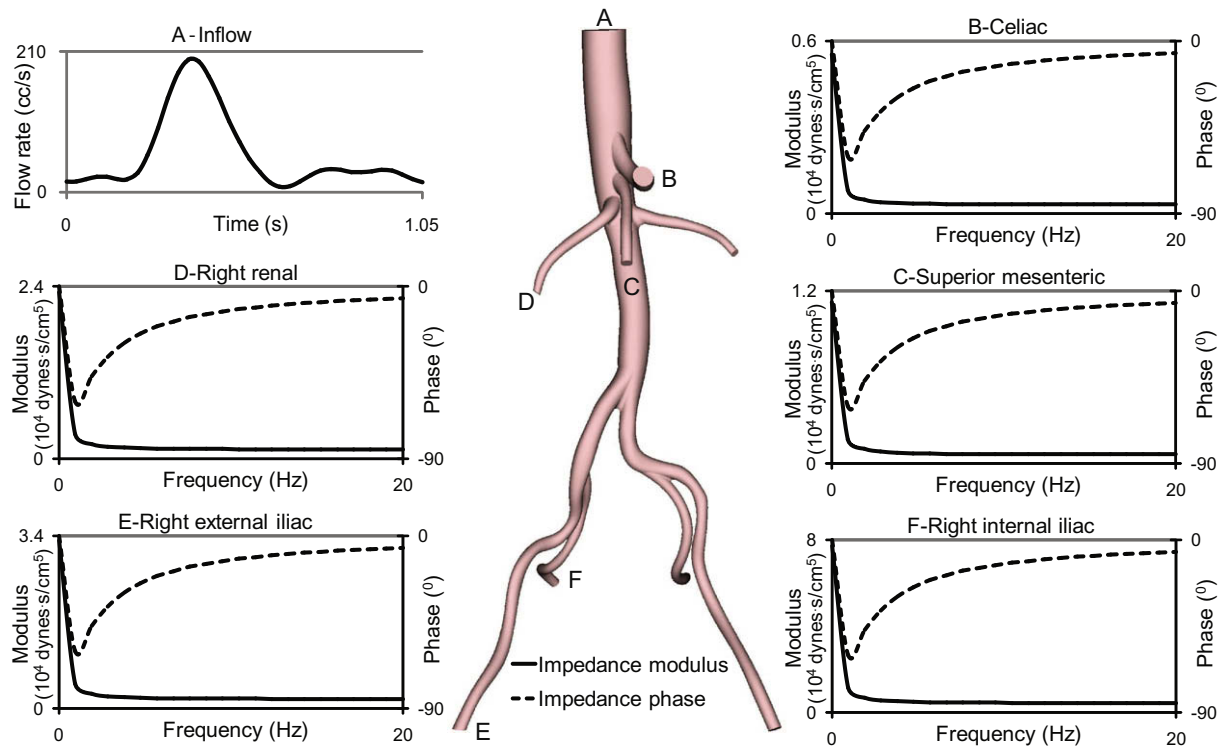


Fig. 4. Boundary conditions for a subject-specific abdominal aorta model. A Womersley velocity profile is prescribed at the inlet (A). At the outlet boundaries, impedance boundary conditions are prescribed. The impedance spectra shown in panels (B)–(F) are generated from a three-element Windkessel model. Note that impedance modulus and phase are shown from 0 to 20 Hz.

$$\begin{aligned} \mathcal{S}_h^m &= \left\{ \vec{v} | \vec{v}(\cdot, t) \in H^1(\Omega)^{n_{sd}}, t \in [0, T], \vec{v}|_{\vec{x} \in \bar{\Omega}_e} \in \mathcal{P}_m(\bar{\Omega}_e)^{n_{sd}}, \vec{v}(\cdot, t) = \vec{g} \text{ on } \Gamma_g \right\}, \\ \mathcal{W}_h^m &= \left\{ \vec{w} | \vec{w}(\cdot, t) \in H^1(\Omega)^{n_{sd}}, t \in [0, T], \vec{w}|_{\vec{x} \in \bar{\Omega}_e} \in \mathcal{P}_m(\bar{\Omega}_e)^{n_{sd}}, \vec{w}(\cdot, t) = \vec{0} \text{ on } \Gamma_g \right\}, \\ \mathcal{P}_h^m &= \left\{ p | p(\cdot, t) \in H^1(\Omega), t \in [0, T], p|_{\vec{x} \in \bar{\Omega}_e} \in \mathcal{P}_m(\bar{\Omega}_e) \right\}, \\ \vec{\lambda}_1(t), \vec{\lambda}_2(t), \dots, \vec{\lambda}_{n_c}(t) &\in (L^2(0, T))^{n_{sd}}, \\ \delta \vec{\lambda}_1(t), \delta \vec{\lambda}_2(t), \dots, \delta \vec{\lambda}_{n_c}(t) &\in (L^2(0, T))^{n_{sd}}, \\ \vec{\kappa}_k \in \mathcal{P}_h^{n_{sd}}, \text{ Penalty numbers where } k &= 1, \dots, n_c, \\ \vec{\sigma}_k \in \mathcal{P}_h^{n_{sd}}, \text{ Regularization parameters such that } |\vec{\sigma}_k| &\ll 1, \quad k = 1, \dots, n_c, \end{aligned} \tag{14}$$

where  $\vec{g}$  is an approximation of  $\vec{g}$  in a discretized spatial domain and  $\mathcal{P}_m(\bar{\Omega}_e)$  is the polynomial space of order  $m$  in  $\bar{\Omega}_e$  (in this study,  $m$  is equal to one).

The Galerkin formulation of the problem is:

Find  $\vec{v} \in \mathcal{S}_h^m$ ,  $p \in \mathcal{P}_h^m$  and  $\vec{\lambda}_1, \vec{\lambda}_2, \dots, \vec{\lambda}_{n_c} \in (L^2(0, T))^{n_{sd}}$  such that for any  $\vec{w} \in \mathcal{W}_h^m$ ,  $q \in \mathcal{P}_h^m$  and  $\delta \vec{\lambda}_1, \delta \vec{\lambda}_2, \dots, \delta \vec{\lambda}_{n_c} \in (L^2(0, T))^{n_{sd}}$  the following is satisfied:

$$\begin{aligned} B_G(\vec{w}, q, \delta \vec{\lambda}_1, \dots, \delta \vec{\lambda}_{n_c}; \vec{v}, p, \vec{\lambda}_1, \dots, \vec{\lambda}_{n_c}) &= \int_{\Omega} \left\{ \vec{w} \cdot (\rho \vec{v}_t + \rho \vec{v} \cdot \nabla \vec{v} - \vec{f}) + \nabla \vec{w} : (-p \vec{I} + \vec{\tau}) \right\} d\vec{x} \\ &\quad - \int_{\Omega} \nabla q \cdot \vec{v} d\vec{x} - \int_{\Gamma_h} \vec{w} \cdot (M_m(\vec{v}, p) + H_m) \cdot \vec{n} ds + \int_{\Gamma_h} q(\vec{M}_c(\vec{v}, p) \\ &\quad + \vec{H}_c) \cdot \vec{n} ds + \int_{\Gamma_g} q \vec{v} \cdot \vec{n} ds \\ &\quad + \sum_{i=1}^{n_{sd}} \sum_{k=1}^{n_c} \{ \lambda_{ki} \cdot (\sigma_{ki} \delta \lambda_{ki} - \delta c_{ki}(\vec{w}; \vec{v}, \vec{x}, t)) \} + \sum_{i=1}^{n_{sd}} \sum_{k=1}^{n_c} \delta \lambda_{ki} \cdot (\sigma_{ki} \lambda_{ki} - c_{ki}(\vec{v}, \vec{x}, t)) \\ &\quad + \sum_{i=1}^{n_{sd}} \sum_{k=1}^{n_c} \kappa_{ki} \cdot c_{ki}(\vec{v}, \vec{x}, t) \delta c_{ki}(\vec{w}; \vec{v}, \vec{x}, t) = 0. \end{aligned} \tag{15}$$

The Stabilized formulation is:

Find  $\vec{v} \in \mathcal{S}_h^m$ ,  $p \in \mathcal{P}_h^m$  and  $\vec{\lambda}_1, \vec{\lambda}_2, \dots, \vec{\lambda}_{n_c} \in (L^2(0, T))^{n_{sd}}$  such that for any  $\vec{w} \in \mathcal{W}_h^m$ ,  $q \in \mathcal{P}_h^m$  and  $\delta \vec{\lambda}_1, \delta \vec{\lambda}_2, \dots, \delta \vec{\lambda}_{n_c} \in (L^2(0, T))^{n_{sd}}$  the following is satisfied:

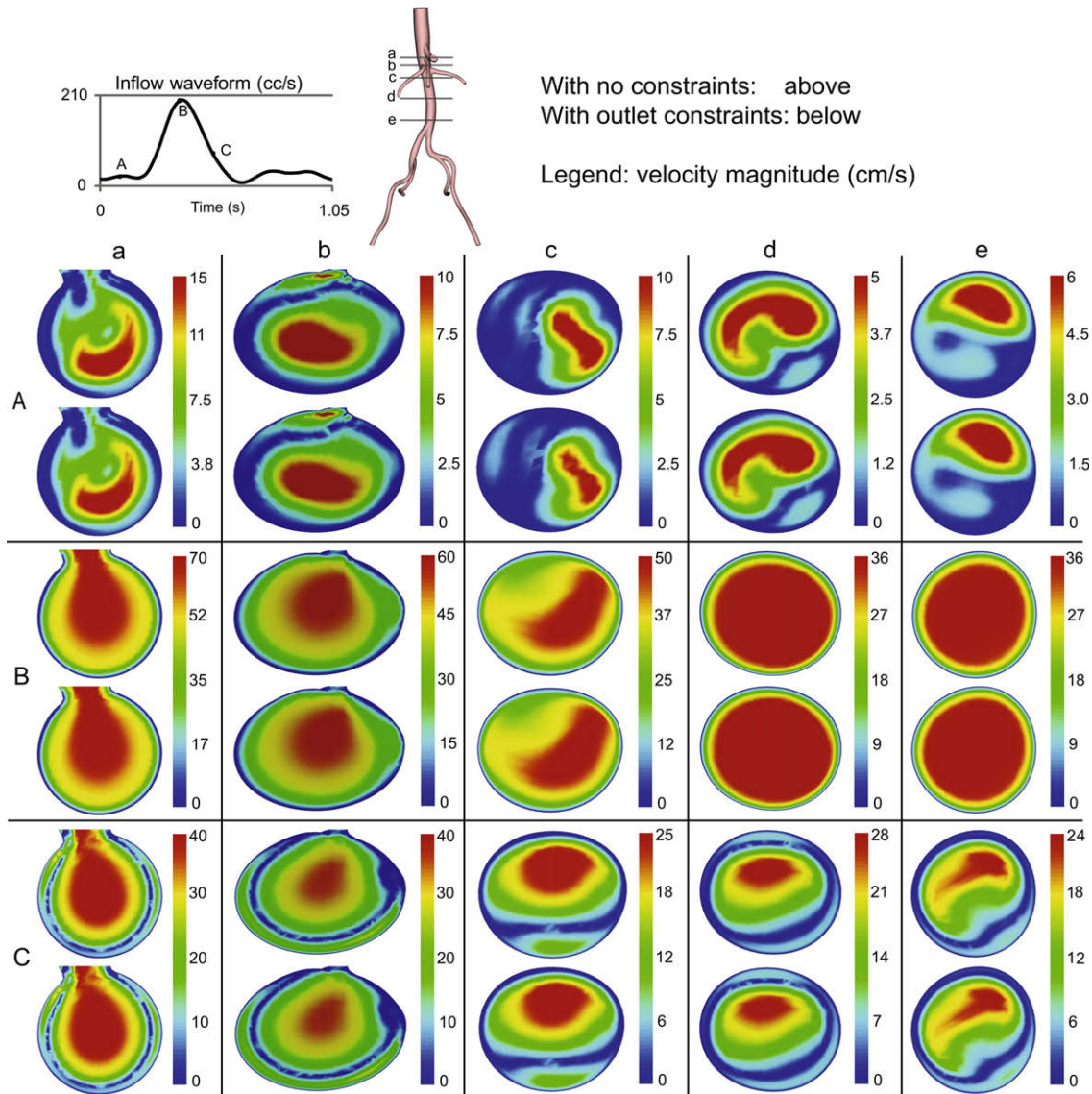
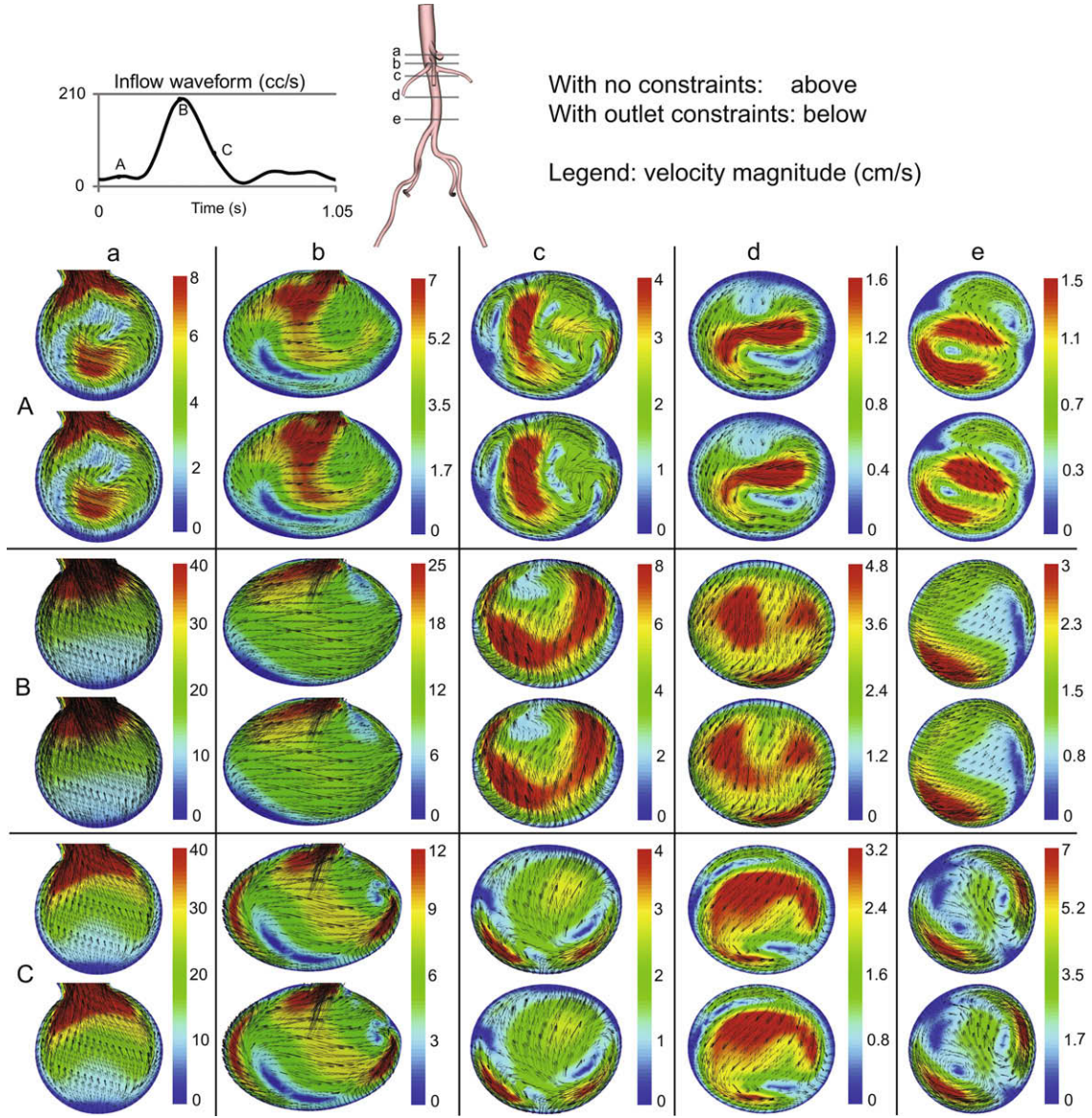


Fig. 5. Through-plane velocity contours at infra-celiac, supra-renal, infra-renal, mid-aorta, and supra-bifurcation locations of a subject-specific abdominal aorta model with a measured inlet flow and impedance outlet boundary conditions. Results are shown for these five axial locations at three time points for simulations without (rows 1, 3, 5) and with (rows 2, 4, 6) constraints on the shape of the outlet velocity profiles.



**Fig. 6.** In-plane velocity vectors and magnitude at infra-celiac, supra-renal, infra-renal, mid-aorta, and supra-bifurcation locations of a subject-specific abdominal aorta model with a measured inlet flow and impedance outlet boundary conditions. Results are shown for these five axial locations at three time points for simulations without (rows 1, 3, 5) and with (rows 2, 4, 6) constraints on the shape of the outlet velocity profiles.

$$\begin{aligned}
 & B_G^S(\vec{w}, q, \delta\vec{\lambda}_1, \dots, \delta\vec{\lambda}_{n_c}; \vec{v}, p, \vec{\lambda}_1, \dots, \vec{\lambda}_{n_c}) \\
 &= B_G(\vec{w}, q, \delta\vec{\lambda}_1, \dots, \delta\vec{\lambda}_{n_c}; \vec{v}, p, \vec{\lambda}_1, \dots, \vec{\lambda}_{n_c}) \\
 &+ \sum_{e=1}^{n_{el}} \int_{\Omega_e} \{ (\vec{v} \cdot \nabla) \vec{w} \cdot \tau_M \vec{\mathcal{L}}(\vec{v}, p) + \nabla \cdot \vec{w} \tau_C \nabla \cdot \vec{v} \} d\vec{x} \\
 &+ \sum_{e=1}^{n_{el}} \int_{\Omega_e} \{ \vec{w} \cdot (\rho \hat{v} \cdot \nabla \vec{v}) + (\vec{\mathcal{L}}(\vec{v}, p) \cdot \nabla \vec{w}) \cdot (\bar{\tau} \vec{\mathcal{L}}(\vec{v}, p) \cdot \nabla \vec{v}) \} d\vec{x} \\
 &+ \sum_{e=1}^{n_{el}} \int_{\Omega_e} \nabla q \cdot \frac{\tau_M}{\rho} \vec{\mathcal{L}}(\vec{v}, p) d\vec{x} = 0, \tag{16}
 \end{aligned}$$

where  $\vec{\mathcal{L}} = \rho \vec{v}_t + \rho \vec{v} \cdot \nabla \vec{v} + \nabla p - \nabla \cdot \tau - \vec{f}$  and  $\hat{v} = -\frac{\tau_M}{\rho} \vec{\mathcal{L}}$ . The stabilization parameters are defined as follows:

$$\begin{aligned}
 \tau_M &= \frac{1}{\sqrt{(2c_1/\Delta t)^2 + \vec{v} \cdot q \vec{v} + c_2 v^2 (q \cdot q)}}, \\
 \tau_C &= \frac{\rho c_{\tau_C}}{8\tau_M \text{tr}(q) c_1} \quad \text{and} \quad \bar{\tau} = \frac{\tau_M}{\sqrt{\vec{\mathcal{L}} \cdot q \cdot \vec{\mathcal{L}}}}. \tag{17}
 \end{aligned}$$

Here,  $c_1$  and  $c_2$  are constants derived from the one-dimensional scalar model problem of the advection–diffusion equation,  $C_{\tau_C}$  is a scale factor for  $\tau_C$ , and  $q$  is the covariant metric tensor:

$$q = (\vec{\zeta}_{\vec{x}})^T \vec{\zeta}_{\vec{x}}. \tag{18}$$

### 2.5. Linearization and time integration algorithms

We can separate the residuals defined in Eq. (16) into momentum, continuity and Lagrange multiplier residuals as follows:

$$\begin{aligned}
 R_m &= \int_{\Omega} \{ \vec{w} \cdot (\rho \vec{v}_t + \rho \vec{v} \cdot \nabla \vec{v} - \vec{f}) + \nabla \vec{w} \cdot (-\rho I + \tau) \} d\vec{x} \\
 &- \int_{\Gamma_h} \vec{w} \cdot (M_m(\vec{v}, p) + H_m) \cdot \vec{n} ds \\
 &- \sum_{i=1}^{n_{sd}} \sum_{k=1}^{n_c} \lambda_{ki} \cdot \delta c_{ki}(\vec{w}; \vec{v}, \vec{x}, t) + \sum_{i=1}^{n_{sd}} \sum_{k=1}^{n_c} \kappa_{ki} \cdot c_{ki}(\vec{v}, \vec{x}, t) \delta c_{ki}(\vec{w}; \vec{v}, \vec{x}, t)
 \end{aligned}$$

$$\begin{aligned}
 & + \sum_{e=1}^{n_{el}} \int_{\Omega_e} \left\{ (\vec{v} \cdot \nabla) \vec{w} \cdot \tau_M \vec{\mathcal{P}}(\vec{v}, p) + \nabla \cdot \vec{w} \tau_c \nabla \cdot \vec{v} \right\} d\vec{x} \\
 & + \sum_{e=1}^{n_{el}} \int_{\Omega_e} \left\{ \vec{w} \cdot (\rho \hat{v} \cdot \nabla \vec{v}) + (\vec{\mathcal{P}}(\vec{v}, p) \cdot \nabla \vec{w}) \cdot (\tau \vec{\mathcal{P}}(\vec{v}, p) \cdot \nabla \vec{v}) \right\} d\vec{x} = 0,
 \end{aligned} \tag{19}$$

$$\begin{aligned}
 R_c = & - \int_{\Omega} \nabla q \cdot \vec{v} d\vec{x} + \int_{\Gamma_h} q(\vec{M}_c(\vec{v}, p) + \vec{H}_c) \cdot \vec{n} ds + \int_{\Gamma_g} q \vec{v} \cdot \vec{n} ds \\
 & + \sum_{e=1}^{n_{el}} \int_{\Omega_e} \nabla q \cdot \frac{\tau_M}{\rho} \vec{\mathcal{P}}(\vec{v}, p) d\vec{x} = 0,
 \end{aligned} \tag{20}$$

$$R_\lambda = \sum_{i=1}^{n_{sd}} \sum_{k=1}^{n_c} \lambda_{ki} \cdot \sigma_{ki} \delta \lambda_{ki} + \sum_{i=1}^{n_{sd}} \sum_{k=1}^{n_c} \delta \lambda_{ki} \cdot (\sigma_{ki} \lambda_{ki} - c_{ki}(\vec{v}, \vec{x}, t)) = 0. \tag{21}$$

Linearization of the residuals with respect to increments in velocity, pressure and Lagrange multipliers results in the following system of linear algebraic equations:

$$\begin{bmatrix} \frac{\partial R_m}{\partial \vec{v}_t} & \frac{\partial R_m}{\partial p_t} & \frac{\partial R_m}{\partial \vec{\lambda}_t} \\ \frac{\partial R_c}{\partial \vec{v}_t} & \frac{\partial R_c}{\partial p_t} & \frac{\partial R_c}{\partial \vec{\lambda}_t} \\ \frac{\partial R_\lambda}{\partial \vec{v}_t} & \frac{\partial R_\lambda}{\partial p_t} & \frac{\partial R_\lambda}{\partial \vec{\lambda}_t} \end{bmatrix}_{t_{n+1}} \begin{bmatrix} \Delta \vec{v}_{t_{n+1}} \\ \Delta p_{t_{n+1}} \\ \Delta \vec{\lambda}_{t_{n+1}} \end{bmatrix} = \begin{bmatrix} -R_m \\ -R_c \\ -R_\lambda \end{bmatrix}_{t_{n+\alpha_f}}. \tag{22}$$

Here,  $\alpha_f$  is a parameter of a Generalized- $\alpha$  method [4,22].

Since the Lagrange multipliers are introduced as additional unknowns, there is a change in the structure of the system of equations. However, because the constraint function only affects the velocity profiles on the constrained surfaces and does not affect the continuity residuals, we have the following:

$$\frac{\partial R_\lambda}{\partial p_t} = \frac{\partial R_c}{\partial \vec{\lambda}_t} = 0.$$

Furthermore, the momentum residuals linearized with the increments of Lagrange multipliers are identical to the Lagrange multiplier residuals linearized with the increments of velocity, thus, the following holds:

$$\frac{\partial R_m}{\partial \vec{\lambda}_t} = \left( \frac{\partial R_\lambda}{\partial \vec{v}_t} \right)^T.$$

We can write the system of linear algebraic equations as follows:

$$\begin{bmatrix} K & -D^T & L^T \\ D & C & 0 \\ L & 0 & M \end{bmatrix} \begin{bmatrix} \Delta \vec{v}_{t_{n+1}} \\ \Delta \vec{p}_{t_{n+1}} \\ \Delta \vec{\lambda}_{t_{n+1}} \end{bmatrix} = \begin{bmatrix} -R_m \\ -R_c \\ -R_\lambda \end{bmatrix}_{t_{n+\alpha_f}}, \tag{23}$$

where  $\Delta \vec{p}_{t_{n+1}} = \frac{\Delta p_{t_{n+1}}}{\alpha_f \gamma}$  and  $\Delta \vec{\lambda}_{t_{n+1}} = \frac{\Delta \lambda_{t_{n+1}}}{\alpha_f \gamma}$ .  $\gamma$  is a parameter of a Generalized- $\alpha$  method [4,22]. Also,  $K \approx \frac{\partial R_m}{\partial \vec{v}_t} \Big|_{t_{n+1}}$ ,  $D \approx \frac{\partial R_c}{\partial \vec{v}_t} \Big|_{t_{n+1}}$ ,  $C \approx \alpha_f \gamma \frac{\partial R_c}{\partial p_t} \Big|_{t_{n+1}}$ ,  $L \approx \frac{\partial R_\lambda}{\partial \vec{v}_t} \Big|_{t_{n+1}}$ , and  $M \approx \alpha_f \gamma \frac{\partial R_\lambda}{\partial \vec{\lambda}_t} \Big|_{t_{n+1}}$ .

The increments of Lagrange multipliers can be computed either simultaneously with the increments of velocity and pressure or decoupled from the system of equations if the same numerical values for regularization parameters  $\sigma_k$  are used for all the constrained outlets where the matrix M reduces to an identity matrix with scaling constant  $\epsilon$  ( $M = \epsilon I$ ) where  $\epsilon = 2\alpha_f \gamma \sigma$ , thus making  $\sigma$  a single regularization parameter.

Using the latter approach, we decouple the increments of the Lagrange multipliers from the system of equations (23) and solve for the increments of velocity and pressure only. We can rewrite the system of equations (23) as the following:

$$\begin{bmatrix} \bar{K} & \bar{L}^T \\ \bar{L} & \epsilon I \end{bmatrix} \begin{bmatrix} \Delta \vec{d}_{t_{n+1}} \\ \Delta \vec{\lambda}_{t_{n+1}} \end{bmatrix} = \begin{bmatrix} -\hat{R} \\ -R_\lambda \end{bmatrix}_{t_{n+\alpha_f}}, \quad \text{where } \bar{K} = \begin{bmatrix} K & -D^T \\ D & C \end{bmatrix}, \\
 \Delta \vec{d}_{t_{n+1}} = \begin{bmatrix} \Delta \vec{v}_{t_{n+1}} \\ \Delta \vec{p}_{t_{n+1}} \end{bmatrix}, \quad \hat{R}|_{t_{n+\alpha_f}} = \begin{bmatrix} R_m \\ R_c \end{bmatrix}_{t_{n+\alpha_f}}, \quad \bar{L} = [L \ 0]. \tag{24}$$

As explained above, the regularization terms are introduced in order to circumvent the formulation of an ill-conditioned system of equations (24). We can express the increments of the Lagrange multipliers as a function of the increments of velocity and pressure as follows:

$$\Delta \vec{\lambda}_{t_{n+1}} = \frac{1}{\epsilon} \left( -R_\lambda|_{t_{n+\alpha_f}} - \bar{L} \Delta \vec{d}_{t_{n+1}} \right). \tag{25}$$

Now, we can solve for the increments of velocity and pressure only by using the following system of equations:

$$\left( \bar{K} - \frac{1}{\epsilon} \bar{L}^T \bar{L} \right) \Delta \vec{d}_{t_{n+1}} = -\hat{R}|_{t_{n+\alpha_f}} + \frac{1}{\epsilon} \bar{L}^T R_\lambda|_{t_{n+\alpha_f}}. \tag{26}$$

This system of equations is solved using two sequential linear iterative methods: the Conjugate Gradient method (CG) and a matrix-free Generalized Minimal RESidual method (GMRES). When computing preconditioning for these two linear iterative methods, additional contributions due to the constraints are considered by adding absolute values of the diagonal components of these additional terms. In the CG method step, approximate pressure values are obtained by solving a discrete pressure Poisson equation [16,54]. Then, using the GMRES method, accurate velocity and pressure values are computed. This algorithm has demonstrated excellent scalability even with the addition of constraint equations. We advance the solutions in time using a Generalized- $\alpha$  method for velocities [4,22] and a Backward Euler method for pressure and

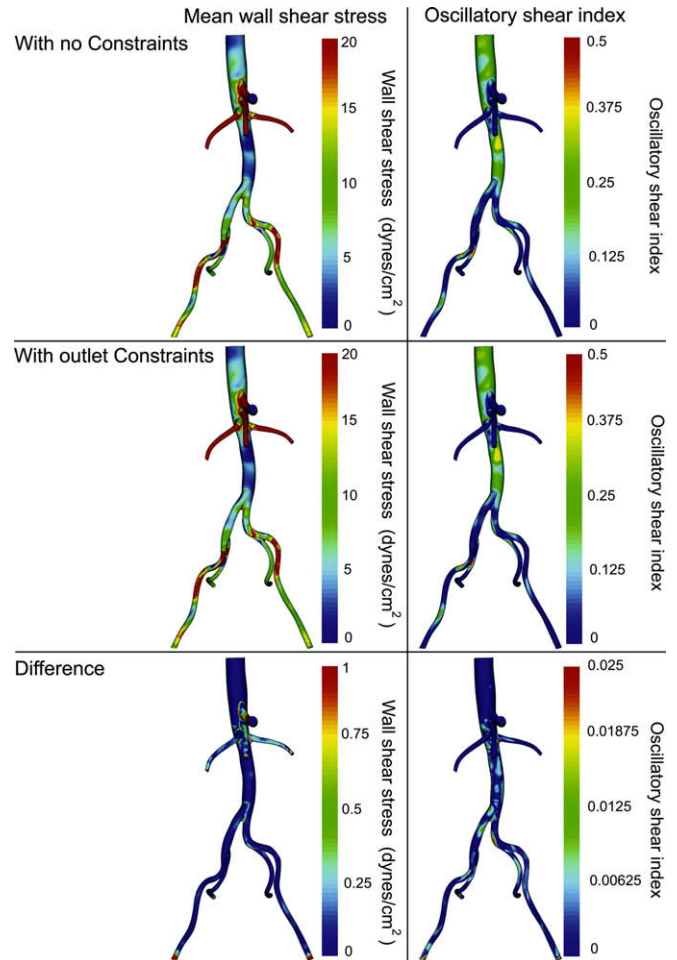


Fig. 7. Mean wall shear stress and oscillatory shear index of a subject-specific abdominal aorta model for simulations with and without constraints on the shape of the outlet velocity profiles.

Lagrange multipliers [22]. The steps of the linearization and time stepping algorithms are summarized below.

1. Set initial conditions:  $\vec{v}(\vec{x}, t_0), p(\vec{x}, t_0), \vec{\lambda}_k(t_0)$  where  $k = 1, \dots, n_c$ .
2. Time step loop: from  $t_n$  to  $t_{n+1}$  where  $n = 0, 1, \dots, N - 1$ . Nonlinear iteration loop: from  $i = 0, 1, \dots, I_{max\_iteration} - 1$ .

(a) Predictor phase

$$\begin{aligned} \vec{v}_{n+1}^{(0)} &= \vec{v}_n, & \vec{v}_{t_{n+1}}^{(0)} &= \frac{\gamma - 1}{\gamma} \vec{v}_{t_n}, \\ p_{n+1}^{(0)} &= p_n, & p_{t_{n+1}}^{(0)} &= 0, \\ \vec{\lambda}_{k,n+1}^{(0)} &= \vec{\lambda}_n, & \vec{\lambda}_{t_{n+1}}^{(0)} &= 0. \end{aligned}$$

(b) Multi-corrector phase

$$\begin{aligned} \vec{v}_{n+\alpha_f}^{(i+1)} &= \vec{v}_n + \alpha_f(\vec{v}_{n+1}^{(i)} - \vec{v}_n), & \vec{v}_{t_{n+\alpha_m}}^{(i+1)} &= \vec{v}_{t_n} + \alpha_m(\vec{v}_{t_{n+1}}^{(i)} - \vec{v}_{t_n}), \\ p_{n+\alpha_f}^{(i+1)} &= p_n + (p_{n+1}^{(i)} - p_n), & p_{t_{n+\alpha_m}}^{(i+1)} &= 0, \\ \vec{\lambda}_{k,n+\alpha_f}^{(i+1)} &= \vec{\lambda}_{k,n} + (\vec{\lambda}_{k,n+1}^{(i)} - \vec{\lambda}_{k,n}), & \vec{\lambda}_{k,t_{n+\alpha_m}}^{(i+1)} &= 0. \end{aligned}$$

(c) Linear solver: solve for  $\Delta \vec{d}_{t_{n+1}}^{(i+1)} = \begin{bmatrix} \Delta \vec{v}_{t_{n+1}}^{(i+1)} \\ \Delta \vec{p}_{t_{n+1}}^{(i+1)} \end{bmatrix}$  and  $\Delta \vec{\lambda}_{t_{n+1}}^{(i+1)}$

- (i) Solve  $(\bar{K} - \frac{1}{\epsilon} \bar{L}^T \bar{L}) \Delta \vec{d}_{t_{n+1}} = -\hat{R}|_{t_{n+\alpha_f}} + \frac{1}{\epsilon} \bar{L}^T R_\lambda|_{t_{n+\alpha_f}}$ 
  - A. Compute preconditioning
  - B. CG method: solve for  $\Delta \vec{p}_{t_{n+1}}^{(i+1)}$  using a discrete pressure Poisson equation [16,54]
  - C. GMRES method: solve for  $\Delta \vec{d}_{t_{n+1}}^{(i+1)}$  using  $(\bar{K} - \frac{1}{\epsilon} \bar{L}^T \bar{L}) \Delta \vec{d}_{t_{n+1}} = -\hat{R}|_{t_{n+\alpha_f}} + \frac{1}{\epsilon} \bar{L}^T R_\lambda|_{t_{n+\alpha_f}}$

(ii) Update  $\vec{\lambda}_{t_{n+1}}^{(i+1)}$  using  $\Delta \vec{\lambda}_{t_{n+1}} = \frac{1}{\epsilon} (-R_\lambda|_{t_{n+\alpha_f}} - \bar{L} \Delta \vec{d}_{t_{n+1}})$

(d) Update phase

$$\begin{aligned} \vec{v}_{n+1}^{(i+1)} &= \vec{v}_{n+1}^{(i)} + \gamma \Delta t \cdot \vec{v}_{t_{n+1}}^{(i+1)}, & \vec{v}_{t_{n+1}}^{(i+1)} &= \vec{v}_{t_{n+1}}^{(i)} + \Delta \vec{v}_{t_{n+1}}^{(i+1)}, \\ p_{n+1}^{(i+1)} &= p_{n+1}^{(i)} + \alpha_f \gamma \Delta t \cdot \Delta \vec{p}_{t_{n+1}}^{(i+1)}, & p_{t_{n+1}}^{(i+1)} &= p_{t_{n+1}}^{(i)} + \alpha_f \gamma \Delta \vec{p}_{t_{n+1}}^{(i+1)}, \\ \vec{\lambda}_{k,n+1}^{(i+1)} &= \vec{\lambda}_{k,n+1}^{(i)} + \alpha_f \gamma \Delta t \cdot \Delta \vec{\lambda}_{k,t_{n+1}}^{(i+1)}, & \vec{\lambda}_{k,t_{n+1}}^{(i+1)} &= \vec{\lambda}_{k,t_{n+1}}^{(i)} + \alpha_f \gamma \Delta \vec{\lambda}_{k,t_{n+1}}^{(i+1)}. \end{aligned}$$

3. Calculate residuals and check for convergence.
4. Conclude at specified time step  $t_N$ .

### 3. Results

For the simulations presented here, we assumed blood can be approximated as an incompressible Newtonian fluid with a density of 1.06 g/cm<sup>3</sup> and a dynamic viscosity of 0.04 g/cm s. Furthermore, we assumed that the vessels are rigid and enforced the no-slip condition at the luminal surface. We utilized anisotropic finite element mesh generation techniques with refinement on exterior surfaces and five boundary layers [37]. The solutions were run until the relative pressure fields and the relative Lagrange multipliers did not change more than 1.0% compared to the solutions from the previous cardiac cycle.

For the inlet boundary conditions, we assigned Womersley velocity profiles derived from flow rate data obtained using cine phase contrast magnetic resonance imaging (cine PC-MRI). For the outlets, we prescribed impedance spectra generated either from fractal networks of linear elastic vessels [32,41] or from three-element Windkessel models. For the simulations with sub-

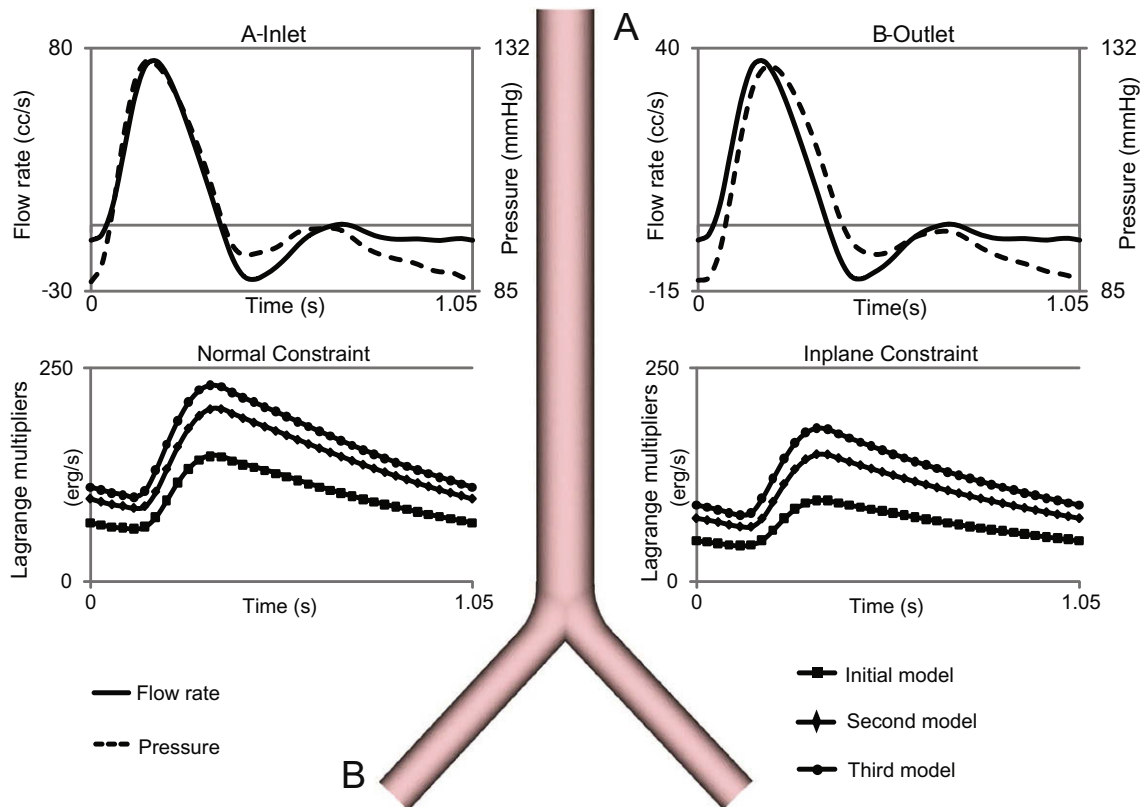


**Fig. 8.** Comparison of Lagrange multipliers of an idealized bifurcation model where daughter vessels are truncated increasingly closer to bifurcation. A Womersley velocity profile is prescribed at the inlet (A) to achieve the volumetric flow rate shown in panel (A). At the outlet boundaries, impedance boundary conditions are used with constraints on the shape of the velocity profiles. Computed inlet pressure and outlet flow and pressure are plotted in panels (A) and (B) respectively.

ject-specific computer models, a target flow distribution to each outlet was determined based on experimental measurements and literature data [19,30,57]. Impedance spectra were adjusted to match this target flow distribution and the measured brachial pulse pressure by adjusting the parameter values of the three-element Windkessel models [26,42]. Outlet velocity profile shapes will be chosen to match the shape of the inlet profile.

### 3.1. A comparison study using a straight cylindrical model

We first applied this method to a straight cylindrical blood vessel model which represents the abdominal aorta of a normal subject. This problem does not require constraints to obtain a solution and therefore is an appropriate example for illustrating the differences between a simulation with and without constraints on the shape of the velocity profile. The nominal radius and vessel length were 1 cm and 22 cm, respectively. For the inlet, we implemented a Womersley velocity profile of a volumetric flow waveform with a mean flow of 3.38 L/min and a cardiac cycle of 1.05 s. For the outlet, we assigned an impedance boundary condition representing the arterial system below the abdominal aorta of a normal subject. The numerical solutions were obtained using a 694,798 element and 124,959 node mesh with a time step size of 1.0 ms for a total of four cardiac cycles.

The shape of the velocity profile on the outlet was constrained using the augmented Lagrangian method. An axisymmetric profile shape with a profile order of five was chosen based on the parameters of the Womersley inlet velocity profile. Finally, the same problem was computed without a constraint on the outlet.

In Fig. 1, the shapes of the velocity profiles from the unconstrained and constrained simulations are compared at five different axial locations. Note that for all axial locations except the outlet, the velocity profiles for the unconstrained and constrained solutions are indistinguishable. When the constraint was applied, the same shape was maintained at the outlet boundary regardless of the magnitude of outlet flow. Flow rate at the outlet surface is not determined a priori but derived naturally through the weak enforcement of the impedance outlet boundary condition.

The inlet pressure waveforms of the simulations performed with and without an outlet velocity profile constraint are compared in Fig. 2. The relative difference of the pressure waveform at the inlet was less than 0.30%. The relative difference in flow and pressure waveforms at the outlet was less than 0.10% and 0.19%, respectively. Similarly, mean wall shear stress and the oscillatory shear index showed little difference except in the immediate vicinity of the outlet (Fig. 3). In Fig. 3, the same problem was run with a different profile order ( $n = 2, 5, 8$ ) to demonstrate that the choice of a profile order is irrelevant to obtain solutions as long as the constrained outlet is far enough from the area of interest.

### 3.2. A comparison study using a subject-specific abdominal aorta model

To further assess the effects of constraints on the shape of the outlet velocity profiles, we analyzed a subject-specific abdominal aorta model (Fig. 4). Once again, this problem does not require constraints to obtain a solution and is used to further illustrate the differences between simulations with and without constraints on the shape of the velocity profiles for a case with multiple outlets. The model starts from the supraceliac level of the abdominal aorta and includes the celiac, superior mesenteric, left renal, right renal, left external iliac, right external iliac, left internal iliac, and right internal iliac arteries. The geometry was obtained from magnetic resonance imaging data. For the inlet, we assigned a Womersley velocity profile. The cardiac cycle of the inlet waveform was 1.05 s. For the outlets, we prescribed impedance spectra generated from Windkessel

models. The solutions were obtained using a 1,943,397 element and 353,314 node mesh with a time step size of 1.0 ms for a total of five cardiac cycles. We examined the worst-case scenario when all the outlets of the model were constrained. An axisymmetric profile function with a profile order of five was chosen based on the parameters of the inlet Womersley velocity profile.

The relative difference in the inlet and outlet pressure between the constrained and unconstrained methods was less than 1.57%. Through-plane velocity contours are compared in Fig. 5. Cut-planes are generated by cutting the computational domain perpendicular to the path line of the abdominal aorta at five different locations: infra-celiac, supra-renal, infra-renal, midway between the renal arteries and iliac bifurcation, and supra-bifurcation. We observe that there is a very small difference in the through-plane velocity contours of the abdominal aorta. The differences observed between the two solutions are comparable to cycle-to-cycle variations of either the unconstrained or the constrained method. The same findings hold for the in-plane velocity components (Fig. 6). Although constraints are imposed on all the outlets, they do not

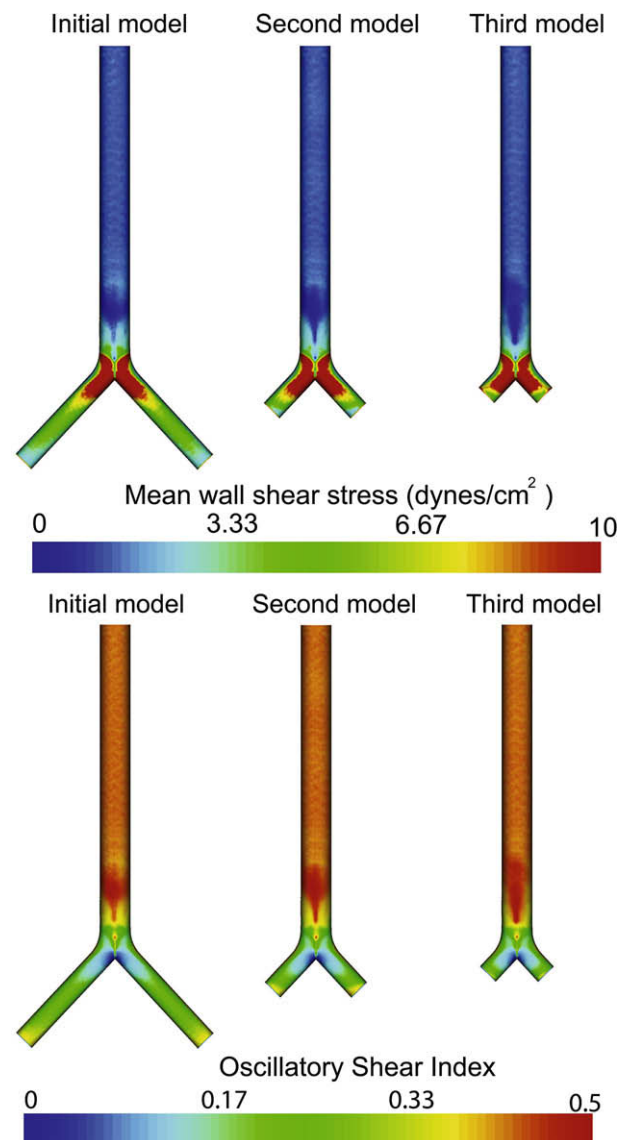


Fig. 9. Comparison of mean wall shear stress and oscillatory shear index of an idealized bifurcation model where daughter vessels are truncated increasingly closer to bifurcation. A Womersley velocity profile is prescribed at the inlet. At the outlet boundaries, impedance boundary conditions are used with constraints on the shape of the velocity profiles.

affect the velocity field in the abdominal aorta. Mean wall shear stress and oscillatory shear index are compared for the unconstrained and constrained methods in Fig. 7. Similarly to the straight cylinder simulation, there is little difference in the wall shear stress except in the branch vessels.

### 3.3. An idealized bifurcation model

An idealized model approximating the bifurcation of the infra-renal aorta into the common iliac arteries was run with constraints on both outlets to study how close the outlet vessels can be truncated without affecting the velocity and pressure fields above the bifurcation. The parent vessel had a nominal radius of 0.67 cm and a length of 13.86 cm. The daughter vessels were constructed to be symmetric with a bifurcation angle of  $90^\circ$ , a radius of 0.47 cm and an initial length of 5.73 cm (Fig. 8). We truncated these outlets until we observed changes in the wall shear stress field above the bifurcation. For the inlet, we assigned a Womersley velocity profile. Note that the prescribed inflow waveform had significant retrograde flow in diastole (Fig. 8). For the outlets, we prescribed impedance spectra which were generated from a three-element Windkessel model. Outlets were constrained with a profile order eleven to approximate the inlet Womersley velocity profile. Initially, the solutions were obtained using a 667,533 element and 121,800 node mesh. The second model was constructed with a shorter daughter vessel length of 2.73 cm. The solutions

were obtained using a 538,932 element and 98,422 node mesh. Finally, the third model was constructed with a daughter vessel length of 1.83 cm and the solutions were obtained using a 513,664 element and 93,837 node mesh. All the simulations were run with a time step size of 1.0 ms for a total of six cardiac cycles. Mesh generation was performed with the same mesh parameters so differences in number of nodes and elements reflect differences in the size of the domain.

In Fig. 8, the flow and pressure waveforms of the inlet and one of the outlets are plotted. Due to the symmetry of the problem, both outlets have the same flow and pressure waveforms. Note that both the inlet and the outlet have significant retrograde flow in diastole. This significant retrograde flow would invariably result in divergence with an unconstrained method, however with the constraints on both outlets, the simulations were successfully run. Furthermore, even though we truncated the outlets very close to the bifurcation for the third model, the simulation did not diverge. When we compared the inlet and outlet pressure waveforms for all three models, the relative inlet and outlet pressure differences were less than 2.23% and 0.21% respectively. Lagrange multipliers for the normal constraint and the in-plane constraints are also plotted in Fig. 8. For the in-plane constraints, the magnitude of the two in-plane constraints is plotted. We can observe that although there is little change in flow and pressure fields, Lagrange multipliers do not preserve the same values but increase for the models with a shorter daughter vessel length to maintain the same

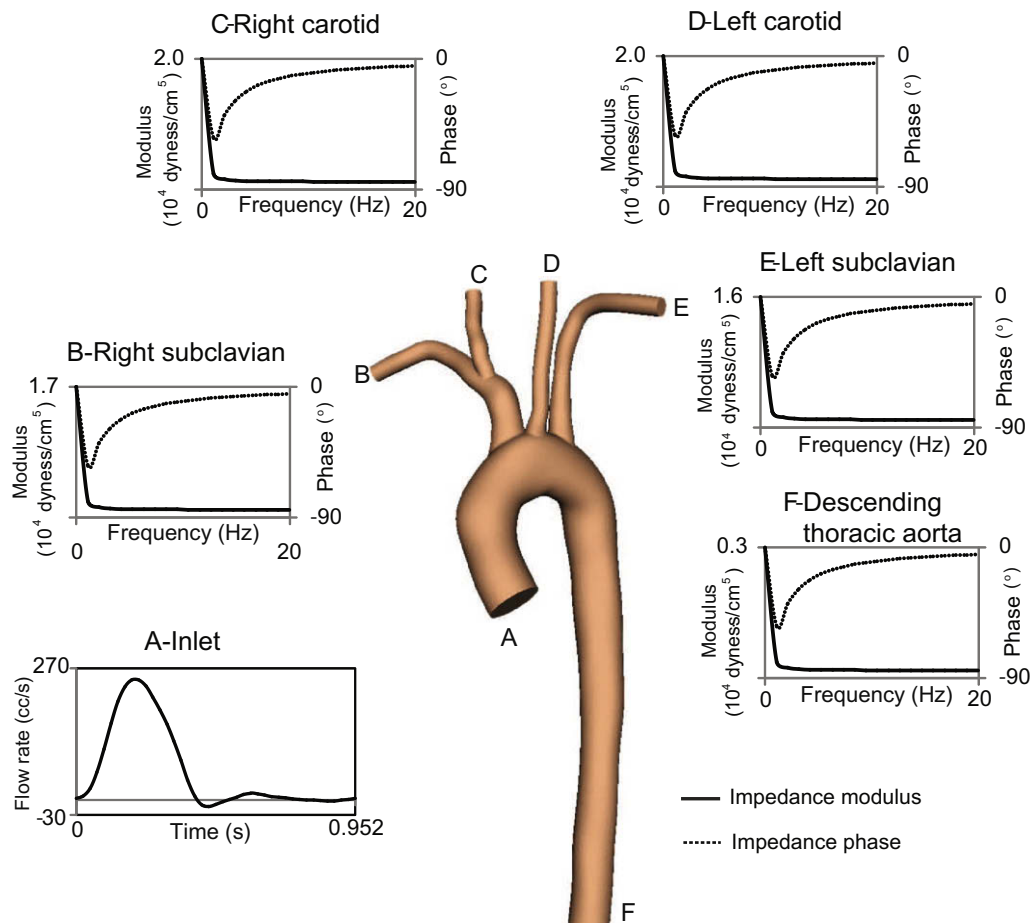


**Fig. 10.** Boundary conditions for a subject-specific thoracic aorta model. A Womersley velocity profile is prescribed at the inlet (A) to achieve the volumetric flow rate shown in panel (A). At the outlet boundaries, a three-element Windkessel boundary conditions are used to generate the impedance spectra shown in (B)–(F). Note that impedance modulus and phase are shown from 0 to 20 Hz.

velocity profiles on the outlets. Lagrange multipliers can be regarded as an artificial force required to maintain a desired shape of the velocity profiles. A model with a shorter daughter vessel length requires a bigger force to maintain the same velocity profile.

To study how the early truncation affects the velocity and pressure fields above the bifurcation, we show mean wall shear stress and oscillatory shear index of three different models (Fig. 9). For the first two models, little difference is observed in the mean shear stress and oscillatory shear index. However, the third model exhibits differences with the initial model in mean shear stress and oscillatory shear index. Although all the models show little difference in velocity and pressure fields at the inlet and both outlets, early truncations such as the third model affect the velocity and pressure fields above the bifurcation. However, up to the second model which has a length-to-radius ratio of 5.81, the velocity and pressure fields above the bifurcation are preserved.

3.4. A subject-specific thoracic aorta model

We applied our new method to a subject-specific thoracic aorta model of an eleven-year-old male subject obtained from magnetic resonance imaging data. This model starts from the root of the aorta, ends above the diaphragm, and includes the following upper, branch vessels: right subclavian, left subclavian, right carotid, and left carotid arteries. The solutions were obtained using a 1,916,167 element and 345,069 node mesh with a time step size of 0.952 ms for six cardiac cycles. The shape of the velocity profiles of all the outlets was constrained to have an axisymmetric shape with a profile order seven to minimize the differences between the prescribed profile function and a fully developed Womersley velocity profile based on the inlet flow rate.

For the inlet boundary condition, we used a Womersley velocity profile and for the outlet boundary conditions, we implemented three-element Windkessel models which represent the downstream vasculature not included in the computational domain. The inflow waveform and impedance spectra generated with a three-element Windkessel model for each outlet are shown in Fig. 10. The measured range of brachial pressure of this subject was 62.5 mmHg in diastole and 106 mmHg in systole. The computed pressure range of the aorta was from 63.0 to 105.0 mmHg. Flow distribution also matched experimental results with a relative difference less than 0.62%.

The solution to this problem diverged without constraints on the outlet boundaries likely due to the fact that all the outlets and the inlet had retrograde flow in early diastole. Prior to solution divergence, the velocity vectors at the outlets became highly irregular (Fig. 11). This simulation was run successfully with constraints on all the outlets.

Fig. 12 shows flow and pressure waveforms of the inlet and the outlets for one cardiac cycle. For the outlets, Lagrange multipliers are plotted. For the in-plane constraints, the magnitude of the two in-plane constraints is plotted. With high flow rate, a small force is sufficient to preserve the shape of the velocity profiles because of the inertia of blood flow. However, for a small amount of outflow, especially in the deceleration phase, a large force is required to maintain the same shape. Therefore, the Lagrange multipliers have large values when there is either a small amount of outflow or retrograde flow, and become smaller when there is positive and high outflow. Note that depending on the location of the outlets, the magnitude of the Lagrange multipliers change. For example, the values of the Lagrange multipliers of the right carotid artery are bigger than the values of the left carotid artery although

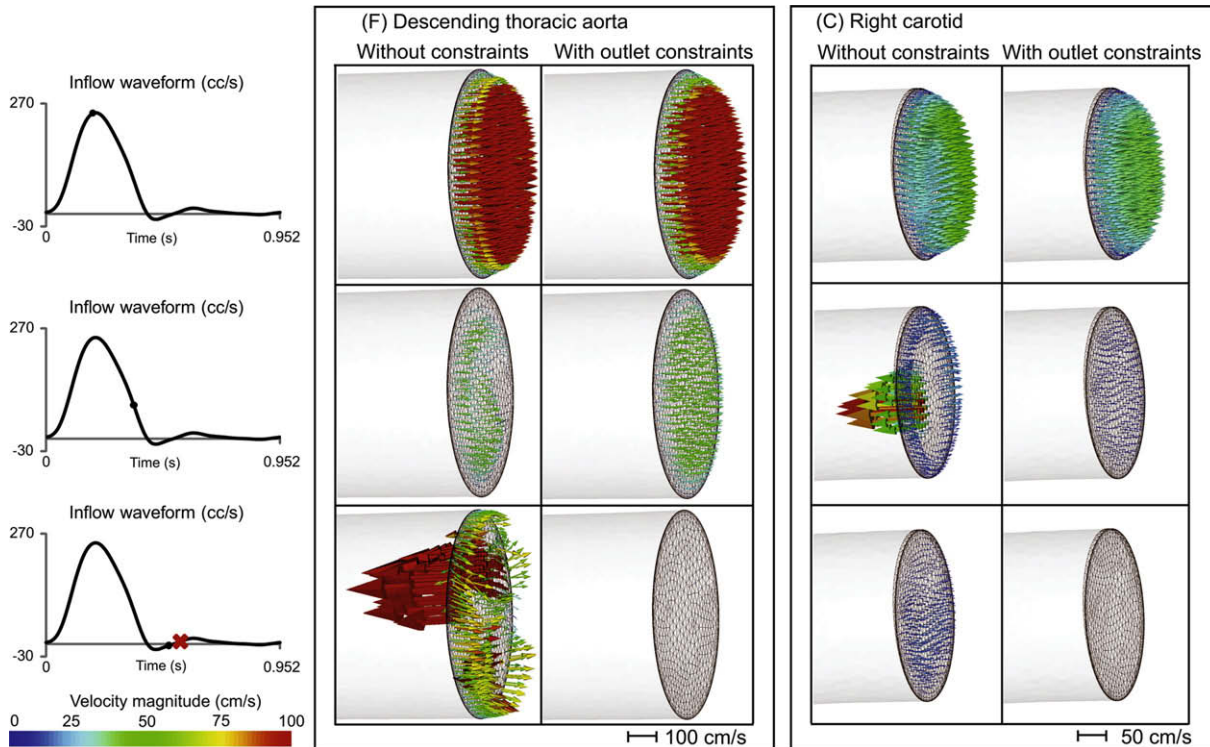
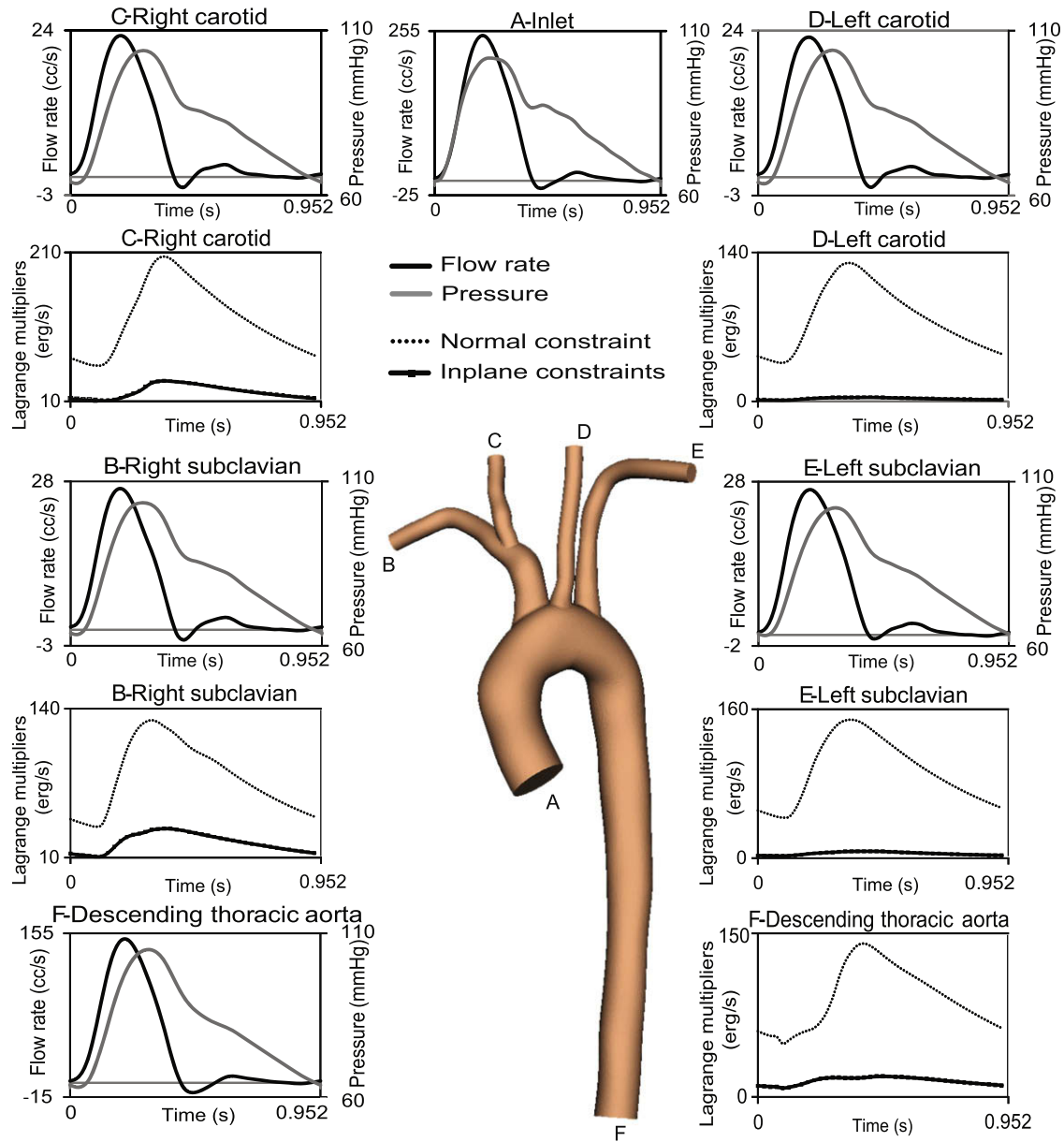


Fig. 11. Velocity vectors at the descending thoracic aorta (F) and right coronary artery (C) of a subject-specific thoracic aorta model. Simulations were performed without and with constraints on the shape of the outlet velocity profiles. Note that the simulation without constraints on the shape of the outlet velocity profiles diverged at the point indicated in a 'x'.



**Fig. 12.** Flow, pressure and Lagrange multipliers of a subject-specific thoracic aorta model. Simulations were performed with constraints on the shape of the outlet velocity profiles. Note that the inlet and all the outlets have reverse flow in early diastole.

they have the same flow because the right carotid artery does not have as long a vessel as the left carotid artery to fully develop flow. Volume rendered velocity magnitudes are shown for peak systole, late systole, and mid-diastole and demonstrate complex flow features in the thoracic aorta (Fig. 13). Due to the geometry of the thoracic aorta, the flow develops helical structures as it travels to the upper branch vessels and descending thoracic aorta. Helical flow structures are preserved up to the immediate vicinity of the outlet surfaces. Wall shear stresses at the same time points are also plotted in Fig. 14. We can observe complex wall shear stress fields due to the complex flow structures.

**4. Discussion**

We have successfully developed and implemented a new method to constrain the shape of the velocity profiles at the interface between a three-dimensional computational domain

and zero-dimensional and one-dimensional analytic models. We have demonstrated that this method exhibits solutions that differ from unconstrained solutions only in the immediate vicinity of the constrained outlets. As long as the constrained outlet is far enough from the domain of interest, the constraints did not affect velocity and pressure fields in the domain of interest. This method can also be used for three-dimensional computations coupled to one-dimensional computational models.

In this method, we used the Coupled Multidomain Method to assign physiologic boundary conditions. There are other approaches to assign physiologic boundary conditions. Some studies use do-nothing boundary conditions [18] and assign weak pressure or flux boundary conditions. These boundary conditions are similar to the Coupled Multidomain Method and do not resolve problems in blood flow simulations associated with complex flow features and geometry. Some boundary conditions prescribe

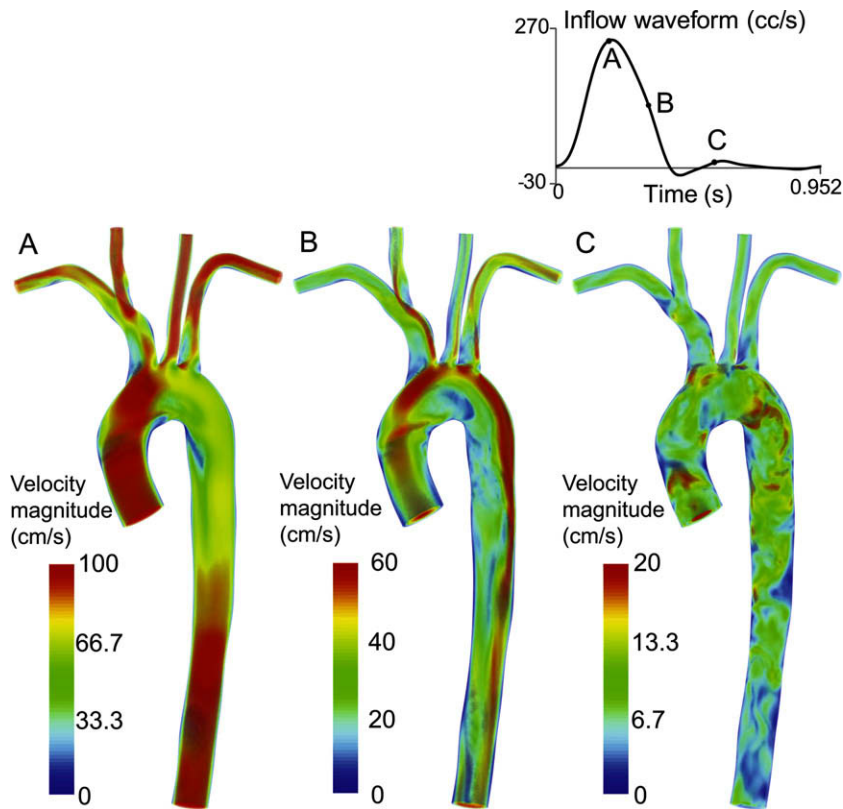


**Fig. 13.** Volume rendered velocity magnitude at peak systole, late systole, and mid-diastole of a subject-specific thoracic aorta model with a prescribed inlet flow and three-element Windkessel outlet boundary conditions and constraints on the shape of the outlet velocity profiles.

either flow rate or pressure using the Augmented formulation [8,49,50] or control theory [11]. However, these approaches are based on the do-nothing approach and thus result in the same natural boundary conditions. Although Gresho et al. [16] demonstrated that these natural boundary conditions are sufficient outlet boundary conditions for incompressible fluid flow, this boundary condition is inadequate for simulations of blood flow in the cardiovascular system when a computational domain is truncated shortly after a bifurcation or where a computational domain has complex flow characteristics such as retrograde flow near the outlets. As our proposed method described herein addresses this issue, it greatly expands the range of problems that can be solved using three-dimensional finite element simulations of blood flow.

We have demonstrated that this method stabilizes unstable problems which are intractable with unconstrained methods. Additionally, the computation cost is comparable to unconstrained methods. Simulation time of the constrained method was compared with the unconstrained method where possible. For the simulations of the straight cylindrical model, two dual cores of a Hitachi Blade Symphony system (Itanium 2 Montecito, 1.6 GHz, 24 MB L3 cache) were used for both methods. With an unconstrained method, the simulation ran for 19.1 h to finish four cardiac cycles. With the constrained method, the same simulation took 20.8 h to finish the same number of cardiac cycles. For a single constraint case, simulation time increased 1.1 times compared to an unconstrained method. When constraining two outlets as in the idealized bifurcation model simulations, the unconstrained method with the initial model took 11.3 h to finish four cardiac cycles with four dual cores of a Hitachi Blade Symphony system whereas

the constrained method ran for 13.6 h to finish the same number of cardiac cycles. The simulation time was 1.2 times greater for a two-constraint case. Finally, when constraining all the outlets as in the simulations of the subject-specific abdominal aorta model, the unconstrained method took 50.9 h to finish five cardiac cycles with six dual cores of the Hitachi Blade Symphony system whereas the constrained method ran for 57.0 h. When constraining all the outlets, the simulation time was 1.1 times greater compared to an unconstrained method. It should be noted that the addition of constraints does not seem to affect the scalability of our algorithm which is near-perfect up to thousands of processors. The computational cost is manageable and necessary as for some class of problems, i.e., those with retrograde diastolic flow, complex flow structures in the neighborhood of outlets or early truncations, an unconstrained approach usually fails.

The increased computational cost due to the addition of constraints on the shape of velocity profiles is primarily from the additional calculations required to formulate the equations. The additional constraint terms are nonlinear and updated before each nonlinear iteration using the most recent velocity and pressure values as well as before each linear iteration using the most recent increments of velocity and pressure.

Finally, the method described here can be extended to other flow problems where weak pressure or flux boundary conditions are implemented to obtain a robust algorithm with better convergence. This method can also be applied at the inlet of three-dimensional computational models to couple the inlet to reduced-order models, for example, a lumped-parameter heart model.

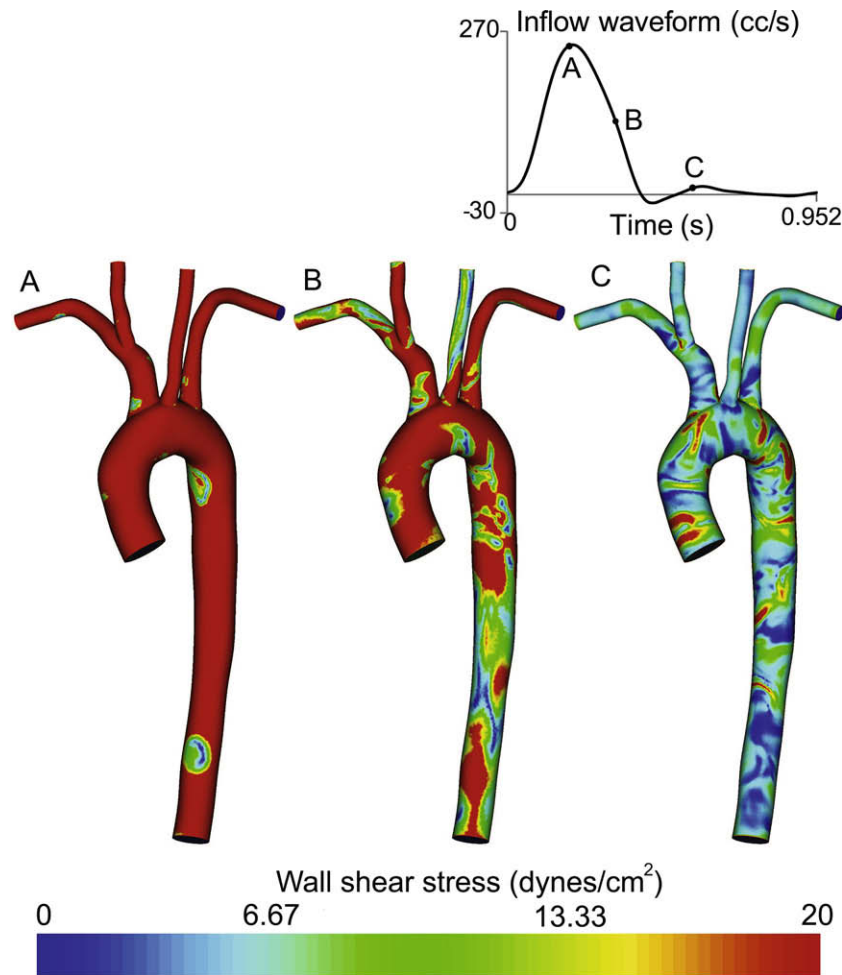


**Fig. 14.** Wall shear stress at peak systole, late systole, and mid-diastole of a subject-specific thoracic aorta model with a prescribed inlet flow and three-element Windkessel outlet boundary conditions and constraints on the shape of the outlet velocity profiles.

## Acknowledgements

Hyun Jin Kim was supported by a Stanford Graduate Fellowship. This material is based upon work supported by the National Science Foundation under Grant No. 0205741. The authors gratefully acknowledge the assistance of Dr. John LaDisa for the construction of the thoracic aorta model and Dr. Nathan Wilson for assistance with software development. The authors gratefully acknowledge Dr. Farzin Shakib for the use of his linear algebra package Acusolve™ (<http://www.acusim.com>) and the support of Simmetrix, Inc. for the use of the MeshSim™ (<http://www.simmetrix.com>) mesh generator.

## References

- [1] P.J. Blanco, R.A. Feijoo, S.A. Urquiza, A unified variational approach for coupling 3D–1D models and its blood flow applications, *Comput. Methods Appl. Mech. Engrg.* 196 (41–44) (2007) 4391–4410.
- [2] A.N. Brooks, T.J.R. Hughes, Streamline upwind Petrov–Galerkin formulation for convection dominated flows with particular emphasis on the incompressible Navier–Stokes equations, *Comput. Methods Appl. Mech. Engrg.* 32 (1982) 199–259.
- [3] J.R. Cebral, M.A. Castro, J.E. Burgess, R.S. Pergolizzi, M.J. Sheridan, C.M. Putman, Characterization of cerebral aneurysms for assessing risk of rupture by using patient-specific computational hemodynamics models, *AJNR Am. J. Neuroradiol.* 26 (10) (2005) 2550–2559.
- [4] J. Chung, G.M. Hulbert, A time integration algorithm for structural dynamics with improved numerical dissipation: the generalized- $\alpha$  method, *J. Appl. Mech.* 60 (1993) 371–375.
- [5] I.M. Cohen, P.K. Kundu, *Fluid Mechanics*, third ed., Cambridge University Press, New York, 2004.
- [6] C.A. Figueroa, I.E. Vignon-Clementel, K.E. Jansen, T.J.R. Hughes, C.A. Taylor, A coupled momentum method for modeling blood flow in three-dimensional deformable arteries, *Comput. Methods Appl. Mech. Engrg.* 195 (41–43) (2006) 5685–5706.
- [7] L. Formaggia, J.F. Gerbeau, F. Nobile, A. Quarteroni, On the coupling of 3D and 1D Navier–Stokes equations for flow problems in compliant vessels, *Comput. Methods Appl. Mech. Engrg.* 191 (2001) 561–582.
- [8] L. Formaggia, J.F. Gerbeau, F. Nobile, A. Quarteroni, Numerical treatment of defective boundary conditions for the Navier–Stokes equations, *SIAM J. Numer. Anal.* 40 (1) (2002) 376–401.
- [9] L. Formaggia, A. Moura, F. Nobile, On the stability of the coupling of 3D and 1D fluid–structure interaction models for blood flow simulations, *Esaim: M2AN* 41 (4) (2007) 743–769.
- [10] L. Formaggia, F. Nobile, A. Quarteroni, A. Veneziani, Multiscale modelling of the circulatory system: a preliminary analysis, *Comput. Visual. Sci.* 2 (2/3) (1999) 75–83.
- [11] L. Formaggia, A. Veneziani, C. Vergara, A new approach to numerical solution of defective boundary value problems in incompressible fluid dynamics, *SIAM J. Numer. Anal.* 46 (6) (2008) 2769–2794.
- [12] A. Fortin, On the imposition of a flowrate by an augmented Lagrangian method, *Commun. Numer. Methods Engrg.* 4 (1988) 835–841.
- [13] L.P. Franca, S.L. Frey, Stabilized finite element methods ii. the incompressible Navier–Stokes equations, *Comput. Methods Appl. Mech. Engrg.* 99 (2–3) (1992) 209–233.
- [14] T. Frauenfelder, M. Lotfey, T. Boehm, S. Wildermuth, Computational fluid dynamics: hemodynamic changes in abdominal aortic aneurysm after stent-graft implantation, *Cardiovasc. Intervent. Radiol.* 29 (4) (2006) 613–623.
- [15] R. Glowinski, P. Le Tallec, *Augmented Lagrangian and operator-splitting methods in nonlinear mechanics*, SIAM Studies in Applied Mathematics, vol. 9, Society for Industrial and Applied Mathematics, Philadelphia, 1989.
- [16] P.M. Gresho, R.L. Sani, *Incompressible Flow and the Finite Element Method*, John Wiley & Sons Ltd., Chichester, 2000.

- [17] M.R. Hestenes, Multiplier and gradient methods, *J. Optimiz. Theory Appl.* 4 (5) (1969) 303–320.
- [18] J. Heywood, R. Rannacher, S. Turek, Artificial boundaries and flux and pressure conditions for the incompressible Navier–Stokes equations, *Int. J. Numer. Methods Fluids* 22 (5) (1996) 325–352.
- [19] S.A. Hope, D.B. Tay, I.T. Meredith, J.D. Cameron, Waveform dispersion, not reflection, may be the major determinant of aortic pressure wave morphology, *Am. J. Physiol. Heart Circ. Physiol.* 289 (6) (2005) H2497–H2502.
- [20] T.J.R. Hughes, J. Lubliner, On the one-dimensional theory of blood flow in the larger vessels, *Math. Biosci.* 18 (1–2) (1973) 161–170.
- [21] T.J.R. Hughes, *The Finite Element Method: Linear Static and Dynamic Finite Element Analysis*, Dover Publications, New York, 2000.
- [22] K.E. Jansen, C.H. Whiting, G.M. Hulbert, Generalized- $\alpha$  method for integrating the filtered Navier–Stokes equations with a stabilized finite element method, *Comput. Methods Appl. Mech. Engrg.* 190 (3–4) (2000) 305–319.
- [23] L.D. Jou, C.M. Quick, W.L. Young, M.T. Lawton, R. Higashida, A. Martin, D. Saloner, Computational approach to quantifying hemodynamic forces in giant cerebral aneurysms, *AJNR Am. J. Neuroradiol.* 24 (9) (2003) 1804–1810.
- [24] J.P. Ku, M.T. Draney, F.R. Arko, W.A. Lee, F.P. Chan, N.J. Pelc, C.K. Zarins, C.A. Taylor, In vivo validation of numerical prediction of blood flow in arterial bypass grafts, *Ann. Biomed. Engrg.* 30 (6) (2002) 743–752.
- [25] K. Lagana, R. Balossino, F. Migliavacca, G. Pennati, E.L. Bove, M.R. de Leval, G. Dubini, Multiscale modeling of the cardiovascular system: application to the study of pulmonary and coronary perfusions in the univentricular circulation, *J. Biomech.* 38 (5) (2005) 1129–1141.
- [26] W.K. Laskey, H.G. Parker, V.A. Ferrari, W.G. Kussmaul, A. Noordergraaf, Estimation of total systemic arterial compliance in humans, *J. Appl. Physiol.* 69 (1) (1990) 112–119.
- [27] Z. Li, C. Kleinstreuer, Blood flow and structure interactions in a stented abdominal aortic aneurysm model, *Med. Engrg. Phys.* 27 (5) (2005) 369–382.
- [28] A.L. Marsden, I.E. Vignon-Clementel, F.P. Chan, J.A. Feinstein, C.A. Taylor, Effects of exercise and respiration on hemodynamic efficiency in CFD simulations of the total cavopulmonary connection, *Ann. Biomed. Engrg.* 35 (2) (2007) 250–263.
- [29] F. Migliavacca, R. Balossino, G. Pennati, G. Dubini, T.Y. Hsia, M.R. de Leval, E.L. Bove, Multiscale modelling in biofluidynamics: application to reconstructive paediatric cardiac surgery, *J. Biomech.* 39 (6) (2006) 1010–1020.
- [30] J.E. Moore, D.N. Ku, Pulsatile velocity measurements in a model of the human abdominal aorta under simulated exercise and postprandial conditions, *J. Biomech. Engrg.* 116 (1) (1994) 107–111.
- [31] J.T. Oden, N. Kikuchi, Finite element methods for constrained problems in elasticity, *Int. J. Numer. Methods Engrg.* 18 (5) (1982) 701–725.
- [32] M.S. Olufsen, Structured tree outflow condition for blood flow in larger systemic arteries, *Am. J. Physiol.* 276 (1999) H257–H268.
- [33] M. Oshima, R. Torii, T. Kobayashi, N. Taniguchi, K. Takagi, Finite element simulation of blood flow in the cerebral artery, *Comput. Methods Appl. Mech. Engrg.* 191 (6–7) (2001) 661–671.
- [34] K. Perktold, R. Peter, M. Resch, Pulsatile non-Newtonian blood flow simulation through a bifurcation with an aneurysm, *Biorheology* 26 (6) (1989) 1011–1030.
- [35] M.J.D. Powell, *A Method for Nonlinear Constraints in Minimization Problems in Optimization*, Academic Press, New York, 1969 [Chapter 19].
- [36] A. Quarteroni, S. Ragni, A. Veneziani, Coupling between lumped and distributed models for blood flow problems, *Comput. Visual. Sci.* 4 (2) (2001) 111–124.
- [37] O. Sahni, J. Muller, K.E. Jansen, M.S. Shephard, C.A. Taylor, Efficient anisotropic adaptive discretization of the cardiovascular system, *Comput. Methods Appl. Mech. Engrg.* 195 (41–43) (2006) 5634–5655.
- [38] E.B. Shim, R.D. Kamm, T. Heldt, R.G. Mark, Numerical analysis of blood flow through a stenosed artery using a coupled multiscale simulation method, *Comput. Cardiol.* (2000) 219–222.
- [39] J.C. Simo, R.L. Taylor, Quasi-incompressible finite elasticity in principal stretches. Continuum basis and numerical algorithms, *Comput. Methods Appl. Mech. Engrg.* 85 (3) (1991) 273–310.
- [40] D.D. Soerensen, K. Pekkan, D. de Zelicourt, S. Sharma, K. Kanter, M. Fogel, A.P. Yoganathan, Introduction of a new optimized total cavopulmonary connection, *Ann. Thorac. Surg.* 83 (6) (2007) 2182–2190.
- [41] B.N. Steele, M.S. Olufsen, C.A. Taylor, Fractal network model for simulating abdominal and lower extremity blood flow during resting and exercise conditions, *Comput. Methods Biomech. Biomed. Engrg.* 10 (1) (2007) 39–51.
- [42] N. Stergiopoulos, P. Segers, N. Westerhof, Use of pulse pressure method for estimating total arterial compliance in vivo, *Am. J. Physiol. Heart Circ. Physiol.* 276 (2) (1999) H424–H428.
- [43] G.R. Stuhne, D.A. Steinman, Finite-element modeling of the hemodynamics of stented aneurysms, *J. Biomech. Engrg.* 126 (3) (2004) 382–387.
- [44] B.T. Tang, C.P. Cheng, M.T. Draney, N.M. Wilson, P.S. Tsao, R.J. Herfkens, C.A. Taylor, Abdominal aortic hemodynamics in young healthy adults at rest and during lower limb exercise: quantification using image-based computer modeling, *Am. J. Physiol. Heart Circ. Physiol.* 291 (2) (2006) H668–H676.
- [45] C.A. Taylor, C.P. Cheng, L.A. Espinosa, B.T. Tang, D. Parker, R.J. Herfkens, In vivo quantification of blood flow and wall shear stress in the human abdominal aorta during lower limb exercise, *Ann. Biomed. Engrg.* 30 (3) (2002) 402–408.
- [46] C.A. Taylor, M.T. Draney, J.P. Ku, D. Parker, B.N. Steele, K. Wang, C.K. Zarins, Predictive medicine: computational techniques in therapeutic decision-making, *Comput. Aided Surg.* 4 (5) (1999) 231–247.
- [47] C.A. Taylor, M.T. Draney, Experimental and computational methods in cardiovascular fluid mechanics, *Annu. Rev. Fluid Mech.* 36 (2004) 197–231.
- [48] C.A. Taylor, T.J.R. Hughes, C.K. Zarins, Finite element modeling of blood flow in arteries, *Comput. Methods Appl. Mech. Engrg.* 158 (1–2) (1998) 155–196.
- [49] A. Veneziani, C. Vergara, Flow rate defective boundary conditions in haemodynamics simulations, *Int. J. Numer. Methods Fluids* 47 (8–9) (2005) 803–1316.
- [50] A. Veneziani, C. Vergara, An approximate method for solving incompressible Navier–Stokes problems with flow rate conditions, *Comput. Methods Appl. Mech. Engrg.* 196 (9–12) (2007) 1685–1700.
- [51] I.E. Vignon-Clementel, C.A. Figueroa, K.E. Jansen, C.A. Taylor, Outflow boundary conditions for three-dimensional finite element modeling of blood flow and pressure in arteries, *Comput. Methods Appl. Mech. Engrg.* 195 (29–32) (2006) 3776–3796.
- [52] I.E. Vignon-Clementel, C.A. Figueroa, K.E. Jansen, C.A. Taylor, Outflow boundary conditions for three-dimensional simulations of non-periodic blood flow and pressure fields in deformable arteries, *Comput. Methods Biomech. Biomed. Engrg.*, in press.
- [53] J.J. Wentzel, F.J.H. Gijzen, J.C.H. Schuurbers, R. Krams, P.W. Serruys, P.J. De Feyter, C.J. Slager, Geometry guided data averaging enables the interpretation of shear stress related plaque development in human coronary arteries, *J. Biomech.* 38 (7) (2005) 1551–1555.
- [54] C.H. Whiting, K.E. Jansen, A stabilized finite element method for the incompressible Navier–Stokes equations using a hierarchical basis, *Int. J. Numer. Methods Fluids* 35 (2001) 93–116.
- [55] J.R. Womersley, *An Elastic Tube Theory of Pulse Transmission and Oscillatory Flow in Mammalian Arteries*, Wright Air Development Center, Wright-Patterson Air Force Base, OH, 1957.
- [56] J.J. Yeung, H.J. Kim, T.A. Abbruzzese, I.E. Vignon-Clementel, M.T. Draney-Blomme, K.K. Yeung, I. Perikash, R.J. Herfkens, C.A. Taylor, R.L. Dalman, Aortoiliac hemodynamic and morphologic adaptation to chronic spinal cord injury, *J. Vasc. Surg.* 44 (6) (2006) 1254–1265.
- [57] M. Zamir, P. Sinclair, T.H. Wonnacott, Relation between diameter and flow in major branches of the arch of the aorta, *J. Biomech.* 25 (11) (1992) 1303–1310.